AGU PUBLICATIONS

Global Biogeochemical Cycles

RESEARCH ARTICLE
10.1002/2016GB005521

Key Points:
- A mechanistic net phytoplankton production (NPP) model that exploits state-of-the-art satellite ocean color analyses is presented
- A comparison to direct NPP field measurements shows higher model skill relative to other published NPP models
- The model predicts global oceanic NPP is 52 Pg C m^{-2} yr^{-1} and suggests that NPP in the oligotrophic gyres has been historically underestimated

Correspondence to:
G. M. Silsbe,
gsilsbe@umces.edu

Citation:
Silsbe, G. M., M. J. Behrenfeld, K. H. Halsey, A. J. Milligan, and T. K. Westberry (2016), The CAFE model: A net production model for global ocean phytoplankton, *Global Biogeochem. Cycles*, *30*, 1756–1777, doi:10.1002/2016GB005521.

Received 6 SEP 2016
Accepted 31 OCT 2016
Accepted article online 3 NOV 2016
Published online 3 DEC 2016

The CAFE model: A net production model for global ocean phytoplankton

Greg M. Silsbe[1,2], Michael J. Behrenfeld[1], Kimberly H. Halsey[3], Allen J. Milligan[1], and Toby K. Westberry[1]

[1]Department of Botany and Plant Pathology, Oregon State University, Corvallis, Oregon, USA, [2]Now at Horn Point Laboratory, University of Maryland Center for Environmental Sciences, Cambridge, Maryland, USA, [3]Department of Microbiology, Oregon State University, Corvallis, Oregon, USA

Abstract The Carbon, Absorption, and Fluorescence Euphotic-resolving (CAFE) net primary production model is an adaptable framework for advancing global ocean productivity assessments by exploiting state-of-the-art satellite ocean color analyses and addressing key physiological and ecological attributes of phytoplankton. Here we present the first implementation of the CAFE model that incorporates inherent optical properties derived from ocean color measurements into a mechanistic and accurate model of phytoplankton growth rates (μ) and net phytoplankton production (NPP). The CAFE model calculates NPP as the product of energy absorption (Q_{PAR}), and the efficiency (ϕ_μ) by which absorbed energy is converted into carbon biomass (C_{Phyto}), while μ is calculated as NPP normalized to C_{Phyto}. The CAFE model performance is evaluated alongside 21 other NPP models against a spatially robust and globally representative set of direct NPP measurements. This analysis demonstrates that the CAFE model explains the greatest amount of variance and has the lowest model bias relative to other NPP models analyzed with this data set. Global oceanic NPP from the CAFE model (52 Pg C m^{-2} yr^{-1}) and mean division rates (0.34 day^{-1}) are derived from climatological satellite data (2002–2014). This manuscript discusses and validates individual CAFE model parameters (e.g., Q_{PAR} and ϕ_μ), provides detailed sensitivity analyses, and compares the CAFE model results and parameterization to other widely cited models.

1. Introduction

Phytoplankton net primary production (NPP) is an important conduit through which inorganic carbon enters aquatic biomes. NPP establishes the carrying capacities of marine ecosystems and ultimately regulates the flux of carbon to the deep ocean (i.e., the "biological pump"). As a vital living link in the carbon cycle, understanding how NPP varies through space, time, and across global climatic oscillations (e.g., El Niño–Southern Oscillation) is a key objective in oceanographic research. Prior to the launch of ocean observing satellites, the primary source of uncertainty in global NPP assessments was the paucity of direct field measurements. Now, through ever-improving satellite capabilities and data analytics, uncertainty is driven by how accurately satellite measurements of ocean color (i.e., radiance) can be scaled to NPP. Converting a radiometric quantity (radiance) to a physiological rate (NPP) is a daunting challenge, as reflected by current global annual NPP estimates which range from 32 to 79 Pg C yr^{-1} [*Carr et al.*, 2006] (for context, annual anthropogenic emissions are ~7.8 Pg C yr^{-1} [*Intergovernmental Panel on Climate Change (IPCC)*, 2013]).

The vast majority of NPP models use the concentration of chlorophyll *a* (Chl *a*) as the central metric of phytoplankton biomass. Chl *a* is empirically related to ocean color, and the accuracy of Chl *a*-based models is largely dependent on their ability to predict phytoplankton carbon assimilation efficiencies (i.e., NPP per unit Chl *a*) [*Behrenfeld and Falkowski*, 1997; *Milutinovic and Bertino*, 2011]. While it has long been recognized that phytoplankton acclimate to their nutrient and light environment through changes in cellular Chl *a* content [*Laws and Bannister*, 1980; *MacIntyre et al.*, 2002], it has been underappreciated how strongly the disparate responses of cellular Chl *a* content are to nutrient and light limitation. The opposing responses of cellular Chl *a* content to nutrient and light limitation confound any simple relationship between NPP and Chl *a* [*Behrenfeld et al.*, 2016].

Through recent advances in ocean color analyses, a range of phytoplankton physiology and biomass metrics beyond Chl *a* can now be retrieved from space. Spectral inversion and bio-optical algorithms now permit retrievals of phytoplankton absorption coefficients $b_{bp}(443\ nm)$ and carbon biomass (C_{Phyto}) from ocean color

[*Lee et al*., 2002; *Maritorena et al*., 2002; *Werdell et al*., 2013; *Behrenfeld et al*., 2005; *Westberry et al*., 2008; *Graff et al*., 2015]. The Carbon, Absorption, and Fluorescence Euphotic-resolving (CAFE) model was introduced by *Westberry and Behrenfeld* [2013] as an adaptable framework for advancing global ocean productivity assessments by exploiting state-of-the-art satellite ocean color analyses while addressing key physiological and ecological attributes of phytoplankton. Here we present the first implementation of the CAFE model that incorporates ocean color measurements into a mechanistic and accurate model of phytoplankton growth rates and NPP. Results of this new model are validated against direct NPP measurements, and global NPP assessments are presented and contrasted against other widely cited models.

1.1. NPP Model Structure

Carbon-based models define NPP as the product of phytoplankton carbon biomass (C_{phyto}) and a growth rate (μ [*Behrenfeld et al.,* 2005, equation (1); *Westberry et al.,* 2008]). These two quantities encapsulate dependencies in several aspects of the phytoplankton growth environment. C_{Phyto} is the standing stock of phytoplankton carbon, reflecting the balance between growth and loss processes, such as grazing by zooplankton, while $E(t,z,\lambda)$ is largely a function of light and nutrient availability. A wealth of culture measurements made across light and nutrient regulated growth rates [e.g., *MacIntyre et al*., 2002] provide robust and well understood empirical relationships between μ and satellite products (Chl *a*, C_{Phyto}, photosynthetic active radiation PAR). Carbon-based NPP models exploit these relationships to derive μ, thus providing a clearer metric of phytoplankton phenology through the disentanglement of predator-prey interactions and physiology [*Behrenfeld and Boss*, 2014].

$$\text{NPP} = C_{\text{Phyto}} \times \mu \tag{1}$$

Absorption-based models define NPP as the product of energy absorption (Q_{PAR}, derived from a_ϕ and PAR), and the efficiency (ϕ_μ) in which absorbed energy is converted into carbon biomass [*Kiefer and Mitchell*, 1983, equation (2); *Antoine and Morel*, 1996; *Lee et al.*, 1996; *Smyth et al*., 2005]. Absorption-based NPP models have several advantages over Chl *a*-based models. First, a_ϕ is directly related to satellite measurements of radiance, whereas empirical models scale radiance to Chl *a*. A round robin evaluation of bio-optical algorithms showed that the accuracy of E_K and Chl *a* retrievals is similar [*Brewin et al*., 2015]. Furthermore, ϕ_μ^{max} retrievals are likely more accurate across different water types [*Lee et al*., 2002], which makes this parameter more suitable for global scale NPP assessments. Absorption-based models also encapsulate accessory pigment composition and packaging effects, thus providing a more complete metric of phytoplankton light harvesting than Chl *a* alone.

$$\text{NPP} = Q_{\text{PAR}} \times \phi_\mu \tag{2}$$

Absorption- and carbon-based modeling approaches can be combined such that μ can be derived mechanistically. Substitution of absorption-based NPP (equation (2)) into equation (1) and solving for μ yields:

$$\mu = Q_{\text{PAR}}/C_{\text{phyto}} \times \phi_\mu \tag{3}$$

Equations (2) and (3) are compact expressions that link rates of energy absorption with primary production and growth. These equations, however, must be expanded in order to accurately incorporate an important aspect of phytoplankton physiology. Satellite-based estimates of Q_{PAR} do not differentiate between absorbed energy that is dissipated as heat (i.e., nonphotochemical quenching, NPQ), re-emitted as fluorescence, or passed to the photosynthetic reaction centers to fuel growth. Partitioning of energy between these pathways is dictated by phytoplankton photoacclimation that imparts a light (E) dependency on ϕ_μ. Absorption-based productivity models account for this E-dependency by not estimating ϕ directly, but rather recognizing this E-dependency is analogous to a photosynthesis-irradiance (PE) curve. Thus, ϕ can be described by two distinct physiological terms, the light saturation parameter E_K and maximum quantum efficiency of growth ϕ_μ^{max}:

$$\phi_\mu = \phi_\mu^{\text{max}} \times \tanh(E_K/E) \tag{4}$$

In this equation, the first term on the right-hand side is the maximum efficiency with which photon energy is converted to growth and it is typically determined in the laboratory and field at low-light levels [*Wozniak et al*., 1992; *Marra et al*., 2007]. The second term on the right-hand side, $\tanh(E_K/E)$ quantifies the decrease

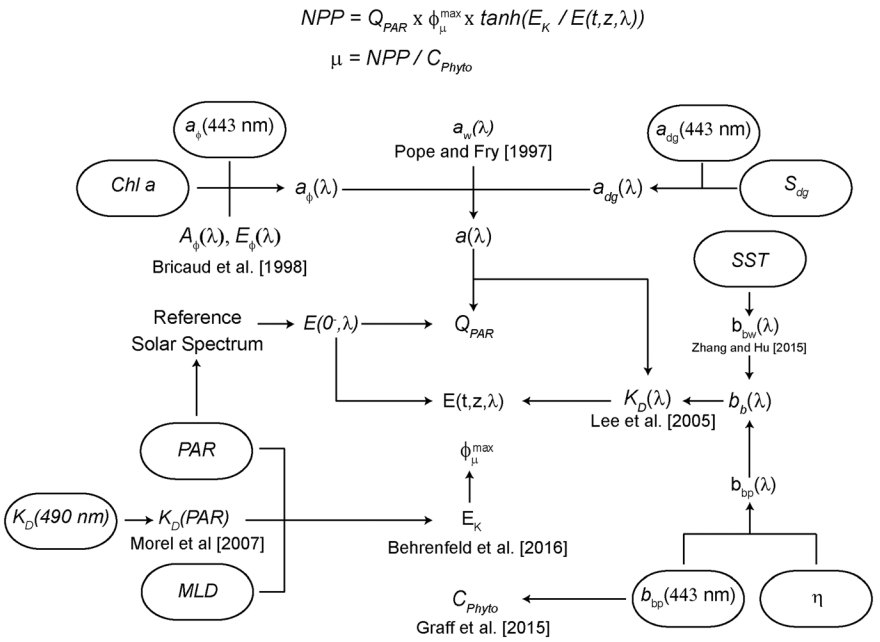

Figure 1. Flowchart summarizing the CAFE model's derivation of NPP and μ. Ovals represent globally gridded data from MODIS-Aqua, except MLD which is taken from http://www.science.oregonstate.edu/ocean.productivity/.

in photosynthetic efficiency as incident light increases. At very low light, the proportion of absorbed energy used for photosynthetic charge separation and electron transport is maximal such that the latter term on the right-hand side of equation (4) has a value of ~1, and NPP is a linear function of absorbed light (thus, the reason $\phi_\mu^{\max}$ is determined from low-light measurements). Substitution of equation (4) into equations (2) and (3) yields

$$\mathrm{NPP} = Q_{\mathrm{PAR}} \times \phi_\mu^{\max} \times \tanh(E_K/E) \tag{5}$$

$$\mu = Q_{\mathrm{PAR}}/C_{\mathrm{phyto}} \times \phi_\mu^{\max} \times \tanh(E_K/E) \tag{6}$$

These revised expressions have a number of advantages. First, advances in ocean color inversion algorithms have allowed significant improvements in the assessment of Q_{PAR}. Second, substantial evidence from the field and laboratory indicates that $\phi_\mu^{\max}$ is relatively constant over a wide range of nutrient and light conditions. Finally, a new description of E_K variability has been developed based on fundamental principles of pigment synthesis regulation [*Behrenfeld et al.*, 2016] that has potential to reduce uncertainties in the final term of equations (5) and (6).

2. Methods

This section first outlines how satellite products are incorporated into the CAFE model to derive NPP and μ (equations (5) and (6)). Figure 1 provides a flowchart of this procedure, and Table 1 lists the symbols, definitions, and units for all relevant terminology. A second subsection then describes the implementation of the CAFE model to assess global NPP and briefly outlines three other published NPP models for comparative analyses. Finally, a third subsection describes how the CAFE model skill is evaluated against a spatially robust set of direct NPP measurements.

2.1. Model Parameterization

A variety of empirical and semianalytical algorithms now permit the derivation of inherent optical properties (IOPs) from satellite imagery [*International Ocean-Colour Coordinating Group*, 2006; *Brewin et al.*, 2015]. All IOP algorithms require a set of assumptions to describe the angular distribution of the in situ light field, and the relative magnitude and spectral shapes of $a_\phi(\lambda)$, the absorption coefficient of detrital and dissolved matter ($a_{\mathrm{dg}}(\lambda)$) with a spectral slope denoted S_{dg}, and the particulate backscattering coefficient ($b_{\mathrm{bp}}(\lambda)$) with a

Table 1. List of Symbols

Data Source Symbol	Definition	Units
	Satellite Data	
a_φ(443 nm)	Phytoplankton absorption coefficient at 443 nm	m^{-1}
a_{dg}(443 nm)	Absorption due to detrital and gelbstoff material at 443 nm	m^{-1}
b_{bp}(443 nm)	Particle backscattering coefficient at 443 nm	m^{-1}
Chl *a*	Chlorophyll *a* concentration	$mg\ m^{-3}$
PAR	Daily integrated photosynthetic active radiation	$mol\ photons\ m^{-2}\ d^{-1}$
SST	Sea surface temperature	°C
S_{dg}	Spectral slope for detrital and gelbstoff absorption	$m^{-1}\ nm^{-1}$
η	Spectral slope for particle backscatter	$m^{-1}\ nm^{-1}$
http://www.science.oregonstate.edu/ocean.productivity/		
MLD	Mixed layer depth	m
	Literature Coefficients	
$a_w(\lambda)$	Absorption due to pure water [*Pope and Fry*, 1997]	m^{-1}
$A.p(\lambda)$, $E.p(\lambda)$	Coefficients defining the spectral shape of $a_\varphi(\lambda)$ [*Bricaud et al.*, 1998]	Dimensionless
m_0, m_1, m_2, m_3	Coefficients for calculating $K_D(\lambda)$ [*Lee et al.*, 2005]	Dimensionless
PARfraction(λ)	Spectral distribution of PAR between 400 and 700 nm	nm^{-1}
	Calculated Data	
a	Absorption coefficient	m^{-1}
$a_\varphi(\lambda)$	Phytoplankton absorption coefficient	m^{-1}
$b_b(\lambda)$	Backscattering coefficient	m^{-1}
$b_{bw}(\lambda)$	Backscattering of pure water	m^{-1}
DL	Day length	day
$E(0^-,\lambda)$	Irradiance below the air-water interface	$mol\ photons\ m^{-2}\ d^{-1}\ nm^{-1}$
$E(t,z,\lambda)$	Irradiance at time *t*, depth *z*, and wavelength λ	$mol\ photons\ m^{-2}\ d^{-1}\ nm^{-1}$
E_K	Light saturation parameter	$mol\ photons\ m^{-2}\ d^{-1}$
$K_D(\lambda)$	Diffuse attenuation coefficient	m^{-1}
I_{ML}	Median mixed layer light level	$mol\ photons\ m^{-2}\ hr^{-1}$
NPP	Net phytoplankton production	$mol\ C\ m^{-2}\ d^{-1}$
$\varphi_\mu(E)$	Light-dependent quantum yield of net carbon fixation	$mol\ C\ (mol\ photons)^{-1}$
φ_μ^{max}	Maximum quantum yield of net carbon fixation	$mol\ C\ (mol\ photons)^{-1}$
θ_Z	Solar zenith angle	Degrees

spectral slope denoted η. Here we use the Generalized Inherent Optical Properties Default Configuration algorithm (GIOP-DC) [*Werdell et al.*, 2013]. In a recent evaluation of IOP algorithm skill using data from the NASA bio-Optical Marine Algorithm Data set [*Brewin et al.*, 2015], the GIOP-DC had the most accurate μ_{max} retrievals and is currently used by NASA's Ocean Biology Processing Group to create archive level satellite IOP products. In the GIOP-DC algorithm the magnitude of $a_\phi(\lambda)$ is unconstrained, but its spectral shape is specified by two Chl *a*-dependent coefficients as presented in *Bricaud et al.* [1998]. These coefficients allow $a_\phi(\lambda)$ to be estimated at 10 nm wavelength (λ) increments using a_ϕ(443 nm) and Chl *a*. In the CAFE model all spectrally dependent parameters are evaluated at 10 nm increments between 400 and 700 nm.

Absorbed energy (Q_{PAR}) is calculated as the product of the daily integrated spectral irradiance just below the seawater interface ($E(0^-,\lambda)$) and the fraction of this energy that is absorbed by phytoplankton ($a_\phi(\lambda)/a(\lambda)$, equation (7)). $E(0^-,\lambda)$ is the product of the satellite-derived daily integrated photosynthetic active radiation (PAR) that is spectrally extrapolated using the ASTMG173 reference spectrum $\left(\int_{\lambda=400\ nm}^{\lambda=700\ nm} \mathrm{PAR.spectrum}(\lambda)\ d\lambda = 1\right)$ and a coefficient 0.95 that approximates the fraction of PAR lost as specular reflectance (equation (8)). Finally, $a(\lambda)$ is calculated as the sum of $a_\phi(\lambda)$, the absorption coefficient of pure water ($a_w(\lambda)$) given in *Pope and Fry* [1997], and $a_{dg}(\lambda)$ computed from a_{dg}(443 nm) and S_{dg}. In the GIOP-DC S_{dg} is constant ($0.018\ m^{-1}$).

$$Q_{PAR} = \int_{\lambda=400\ nm}^{\lambda=700\ nm} E(0^-,\lambda) \times a_\phi(\lambda)/a(\lambda) d\lambda \quad (7)$$

$$E(0^-,\lambda) = \mathrm{PAR} \times \mathrm{PAR.spectrum}(\lambda) \times 0.95 \quad (8)$$

The attenuation coefficient of downwelling irradiance ($K_D(\lambda)$) is calculated using the semianalytical method of *Lee et al.* [2005, equation (9)]. In equation (9) m_0, m_1, m_2, and m_3 are empirically derived coefficients, where m_0

varies with solar zenith angle (θ_Z). $b_b(\lambda)$ is calculated as the sum of $b_{bp}(\lambda)$ and backscattering by pure water ($b_{bw}(\lambda)$), where $b_{bp}(\lambda)$ is calculated from $b_{bp}(443\ \text{nm})$ and η, and $b_{bw}(\lambda)$ is derived as a function of sea surface temperature (SST) and salinity following *Zhang and Hu* [2009]. For simplicity, we assume a constant salinity equal to 32.5 practical salinity unit. $E(t,z,\lambda)$ is derived from $K_D(\lambda)$ and $E(0^-,\lambda)$ following the Beer-Lambert law (equation (10)). In equation (10), z is divided into 101 vertical increments from the surface to Z_{eu}, and t is divided into 101 increments where 0 is sunrise and 1 is sunset. Finally, to convert downwelling planar irradiance to scalar irradiance, $E(t,z,\lambda)$ is multiplied by a factor E_u. E_u is calculated following equation (11) such that the depth, time, and wavelength integration of absorbed energy ($E(t,z,\lambda)\times a_\phi(\lambda)$) equals Q_{PAR} calculated in equation (7). On average, E_u is approximately 1.4 which is consistent with underwater radiative transfer simulations [*Westberry and Siegel*, 2003].

$$K_D(\lambda) = m_0 \times a(\lambda) + m_1 \times \left[1 - m_2 \times \exp^{(-m_3 \times a(\lambda))}\right] \times b_b(\lambda) \tag{9}$$

$$E(t,z,\lambda) = 2\pi \times E(0^-,\lambda) \times \sin(\pi \times t) \times exp^{(-K_D(\lambda)\times z)} \times E_u \tag{10}$$

$$E_\mu = Q_{PAR} / \int_{z=0}^{z=Z_{eu}} \int_{t=0}^{t=1} \int_{400\ nm}^{700\ nm} E(t,z,\lambda) \times a_\phi(\lambda)\ \mathrm{d}\lambda\ \mathrm{d}t\ \mathrm{d}z \tag{11}$$

The next step in the model is calculating the efficiency with which absorbed energy is converted into carbon biomass. The light dependency of ϕ_μ is given in equation (12) and is analogous to a traditional photosynthetic irradiance curve [*Silsbe and Kromkamp*, 2012]. In low light the efficiency in which absorbed energy is converted to carbon biomass is maximal $\left(\phi_\mu^{max}\right)$, then decreases with increasing light as defined by the hyperbolic tangent of the light saturation parameter E_K normalized to irradiance ($E(t,z,\lambda)$). E_K is estimated following the photoacclimation model of *Behrenfeld et al.* [2016]. This E_K model is based on fundamental principles of pigment synthesis regulation and differs depending on whether the mixed layer depth (MLD) extends beyond (equation (13)) or is shallower than (equation (14)) the euphotic depth (Z_{eu}). In these equations PAR is daily integrated surface irradiance, DL is day length, I_{ML} is the median light in the mixed layer (equation (15)), and 0.0864 converts μmol photons $sm^{-2}\,s^{-1}$ to mol photons $m^{-2}\,d^{-1}$. To account for changes in the spectral quality of light through depth, E_K is multiplied by a spectral correction factor following Markager and Vincent [*Markager and Vincent*, 2001, equation (16)]. The inclusion of this spectral correction factor is such that ϕ_μ does not vary with light per se but rather varies with absorbed energy [*Antoine and Morel*, 1996]. Finally, the maximum quantum efficiency of growth ϕ_μ^{max} is modeled as a linear function of E_K between 10 and 150 μmol photons $m^{-2}\,s^{-1}$, with corresponding ϕ_μ^{max} values of 0.030 and 0.018 mol C mol photons^{-1}. This parameterization is consistent with the negative covariance of E_K and ϕ_μ^{max} in field data sets ($r = -0.45$ [*Uitz et al.*, 2008]).

$$\phi_\mu(E) = \phi_\mu^{max} \times \tanh(E_K(z)/E(t,z,\lambda)) \tag{12}$$

$$E_k(\mathrm{MLD} > Z_{eu}) = 0.0864 \times \left(19 \times \exp^{\left(0.038\ \times\ PAR/DL^{0.45}\right)/K_D(\mathrm{PAR})}\right) \tag{13}$$

$$E_k(\mathrm{MLD} \leq Z_{eu}) = 0.0864 \times \left(19 \times \exp^{\left(0.038\ \times\ PAR/DL^{0.45}\right)/K_D(\mathrm{PAR})} \times \frac{1 + \exp^{(-0.15\ \times\ \mathrm{PAR/DL})}}{1 + \exp^{(-3\ \times\ I_{ML})}}\right) \tag{14}$$

$$I_{ML} = \mathrm{PAR/DL} \times \exp^{(-0.5\ \times\ K_D(\mathrm{PAR})\ \times\ \mathrm{MLD})} \tag{15}$$

$$E_K(z) = E_k(z) \times \int_{400\ nm}^{700\ nm} E(t,z,\lambda)\mathrm{d}\lambda \times \int_{400\ nm}^{700\ nm} a_\phi(\lambda)\mathrm{d}\lambda \div \int_{400\ nm}^{700\ nm} E(t,z,\lambda) \times a_\phi(\lambda)\ \mathrm{d}\lambda \tag{16}$$

A significant fraction of phytoplankton biomass can reside beneath the mixed layer depth (MLD), yet still within the euphotic zone. In these low-light environments hidden from satellite imagery, photoacclimation imparts a distinct and pervasive physiological signature. Phytoplankton beneath the surface mixed layer have an increased cellular capacity to absorb light (i.e., higher a_ϕ/C_{phyto}), which in turn decreases E_K relative to surface values [*Cullen*, 2015]. The E_K model adopted here [*Behrenfeld et al.*, 2016] is applicable to surface mixed layer phytoplankton populations only. Therefore, a simple depth dependency to E_K is introduced here for $z >$ MLD. This dependency predicts that E_K decreases exponentially with depth (i.e., proportional to $E(t,z,\lambda)$) to a minimum value of 0.0864 mol photons $m^{-2}\,d^{-1}$ (10 μmol $m^{-2}\,s^{-1}$) when $E(t,z,\lambda)$ reaches 0.1 mol photons $m^{-2}\,d^{-1}$ (equation (17), E_K remains at 10 umol $m^{-2}\,s^{-1}$ at light levels below 0.1 mol photons $m^{-2}\,d^{-1}$). These values were chosen as the approximate lower E_K limit observed in field data

sets [*Huot et al*., 2008] and the minimum daily irradiance that corresponds to deep chlorophyll maxima [*Mignot et al*., 2014], respectively. Estimating phytoplankton biomass and light-harvesting capacity beneath the surface mixed layer is a common challenge of all models. Global analyses of the vertical structure of Chl *a* have shown that on average and consistent with photoacclimation, Chl *a* increases toward the base of the euphotic zone [*Morel and Berthon*, 1989; *Uitz et al*., 2006]. The CAFE model therefore assumes $a_\phi(z > \mathrm{MLD})$ covaries with changes in $E_k(z > \mathrm{MLD})$ (equation (18)). For example, twofold and fourfold decreases in E_K beneath the MLD corresponds to 1.3-fold and 1.6-fold increases in a_ϕ, respectively. For depths beneath the mixed layer but within the euphotic depth, $K_D(\lambda)$, $E(t,z,\lambda)$, and Q_{PAR} were recalculated using $a_\phi(z > \mathrm{MLD})$.

$$E_k(z > \mathrm{MLD}) = 0.0864 + \frac{E_k(\mathrm{MLD}) - 0.0864}{E(\mathrm{MLD}) - 0.1} \times (E(z) - 0.1) \tag{17}$$

$$a_\phi(z > \mathrm{MLD}) = a_\phi(\mathrm{MLD}) \times [1 + 0.15 \times E_k(\mathrm{MLD})/E_k(z > \mathrm{MLD})] \tag{18}$$

2.2. Reassessment of Global NPP, Model Comparisons, and Sensitivity Analyses

NPP estimates from the CAFE model are compared to three other widely cited NPP models. Here we provide a brief overview of each model, and the reader is referred to the original publications for complete model parameterizations. The first model is the wavelength and depth-integrated Chl *a*-based Vertically Generalized Productivity Model [*Behrenfeld and Falkowski*, 1997], herein denoted VGPM. Shown in equation (19), the VGPM derives NPP as the product of the maximum photosynthetic assimilation efficiency $\left(P^B_{\mathrm{opt}}\right)$ which is estimated as a seventh-order polynomial of sea surface temperature (SST), the Chl *a* concentration at the depth where P^B_{opt} occurs, an asymptotic factor of PAR, as well as Z_{eu} and DL. The second model is the chlorophyll-based model of *Antoine and Morel* [1996], herein denoted AM96. AM96 is conceptually similar to an absorption-based model but was published before direct absorption estimates were available from satellite measurements. Shown in equation (20), a_ϕ is derived as the product Chl and the maximum chlorophyll specific absorption coefficient $\left(a^*_{\mathrm{max}}\right)$, where the product of a^*_{max} and ϕ^{max}_μ is assumed to be globally constant, and E_K (denoted K_{PUR} in the original publication) is modeled as a function of SST. The third model is the carbon-based model of *Westberry et al.* [2008], herein denoted CbPM. Shown in equation (21), CbPM derives NPP as the product of C_{phyto} and μ (i.e., equation (1)), where μ is empirically derived as a function of a maximum carbon specific growth rate ($\mu_{\mathrm{max}} = 2\,\mathrm{day}^{-1}$), $\mathrm{Chl}:C_{\mathrm{phyto}}$ as measured from satellite data, and *Chla*.

$$\mathrm{VGPM}: \ \mathrm{NPP} = 0.66125 \times P^B_{\mathrm{opt}}\{\mathrm{SST}\} \times \mathrm{Chl}_{\mathrm{opt}} \times \mathrm{PAR}/(\mathrm{PAR} + 4.1) \times Z_{\mathrm{eu}} \times \mathrm{DL} \tag{19}$$

$$\mathrm{AM96}: \ \mathrm{NPP} = \mathrm{Chl} \times a^*_{\mathrm{max}} \times \phi^\mu_{\mathrm{max}} \times \tanh(E_K\{\mathrm{SST}\}/E) \tag{20}$$

$$\mathrm{CBPM}: \mathrm{NPP} = C_{\mathrm{phyto}} \times \mu\left\{\mu_{\mathrm{max}},\ \mathrm{Chl}:C_{\mathrm{phyto}}, I_{\mathrm{ML}}\right\} \tag{21}$$

Models are compared at global scales and also five specific regions of interest shown in Figure 2. Following *Westberry et al.* [2016], two of these regions represent the high latitude bloom forming Pacific Ocean (NPT: 140°W–150°W, 45°N–50°N) and Atlantic Ocean (NAT: 25°W–35°W, 45°N–50°N). The other three regions are the North Atlantic subtropical gyre (NAG: 25°W–70°W, 25°N–35°N), the South Pacific subtropical gyre (SPG: 90°W–150°W, 15°S–40°S), and the Southern Ocean (SO:>60°S–90°S).

Finally, sensitivity analyses are performed at the global annual scale following *Antoine and Morel* [1996]. Specifically, different components of the CAFE model are adjusted (e.g., E_k is increased 10%), the model is rerun, and annual NPP is computed. To illustrate the spatial impacts of sensitivity analysis model runs, global annual NPP is further partitioned zonally.

2.3. Model Validation

The Primary Production Algorithm Round Robin (PPARR) evaluation is a series of open-community studies to quantify and compare NPP model performance against direct field measurements [*Friedrichs et al*., 2009; *Saba et al*., 2010; *Saba et al*., 2011; *Y. J. Lee et al*., 2015]. Overall, model performance in PPARR studies is quantified using the root-mean-square difference (RMSD, equation (22)), where $\mathrm{NPP}_{\mathrm{mod}}$ and $\mathrm{NPP}_{\mathrm{obs}}$ are modeled and measured NPP, respectively. The RMSD test statistic incorporates both model bias (equation (23)), which quantifies the difference between the average $\mathrm{NPP}_{\mathrm{mod}}$ and $\mathrm{NPP}_{\mathrm{obs}}$, and the unbiased RMSD (uRMSD,

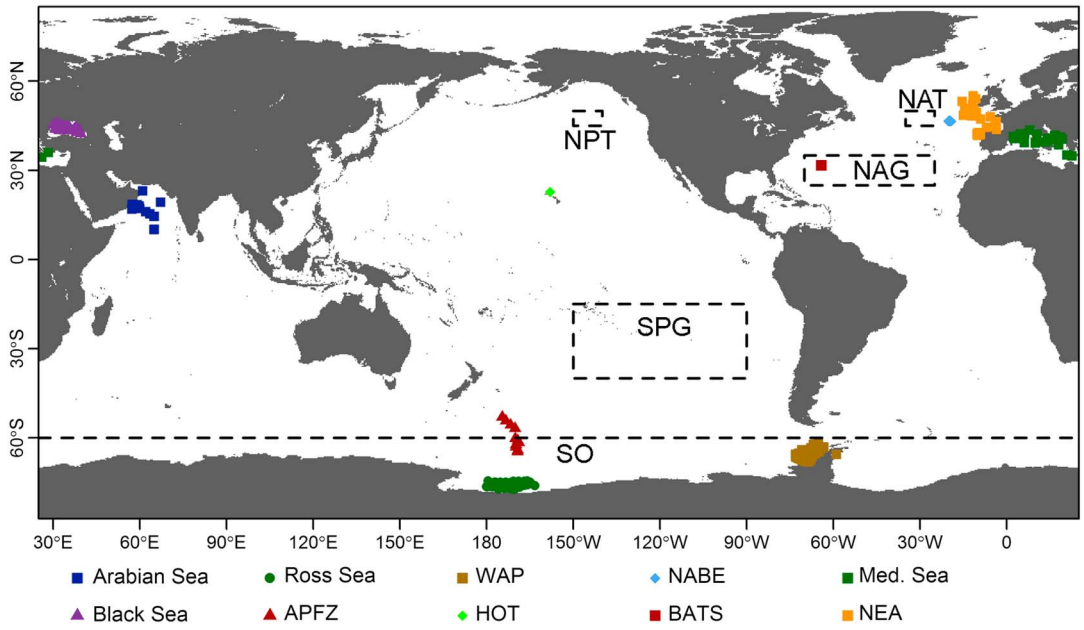

Figure 2. Geographical distribution of in situ NPP data sets used to test model skill are shown as points. Dashed grey boxes delineate regions where seasonality of modeled data is examined (NPT: North Pacific temperate; SPG: South Pacific Gyre; SO: Southern Ocean, NAT: North Atlantic temperate; NAG: North Atlantic Gyre).

equation (24)), which quantifies the ability of modeled NPP to track measured variance. Here these three test statistics are employed to evaluate the CAFE model performance against a large and globally comprehensive PPARR data set [*Saba et al.*, 2011] that is comprised of field NPP measurements from 10 marine regions (Figure 2). The CAFE model is evaluated in each unique region and all regions combined, and results are compared against the 21 other NPP models that are analyzed by *Saba et al.* [2011].

In all PPARR assessments including *Saba et al.* [2011], participating models do not derive NPP from satellite data but rather from a suite of field-measured input data (Chl *a*, PAR, MLD, SST, date, location, and day length) measured alongside NPP. The provision of input data eliminates any bias arising from ocean color retrievals and permits models to be evaluated against NPP measurements where no satellite data are available (e.g., cloud masked data and dates outside the satellite record). As attendant $a_\phi(\lambda)$, $a_{dg}(\lambda)$, $b_b(\lambda)$, and η measurements are not included in the field-measured input data, the CAFE model was modified for this exercise. First, $a_\phi(\lambda)$ was derived as a function of Chl *a* and two wavelength-specific coefficients derived from the global analysis of *Bricaud et al.* [1998, equation (25)]. The influence of this assumption on CAFE model validation is addressed in section 4. Briefly, this assumption likely degrades model performance such that model skill estimates are conservative. Second, $a_{dg}(\lambda)$, $b_b(\lambda)$, and η measurements were derived from climatology measurements for the given month and location (27 km^2 search grid) of the input data. Across the entire *Saba et al.* [2011] data set, climatological data could not be assessed for 9% of the data (predominantly coastal measurements) and are omitted from this analysis.

$$\mathrm{RMSD} = \left(\frac{1}{N}\sum_{i=1}^{N}\left(log_{10}(\mathrm{NPP}_{\mathrm{mod}}(i)) - \log_{10}(\mathrm{NPP}_{\mathrm{obs}}(i))\right)^2\right)^{0.5} \quad (22)$$

$$\mathrm{Bias} = \overline{\log_{10}(\mathrm{NPP}_{\mathrm{mod}})} - \overline{\log_{10}(\mathrm{NPP}_{\mathrm{obs}})} \quad (23)$$

$$\mathrm{uRMSD} = \left(\mathrm{RMSD}^2 - \mathrm{Bias}^2\right)^{0.5} \quad (24)$$

$$a_\phi(\lambda) = A.p(\lambda) \times \mathrm{chl}^{E.p(\lambda)} \quad (25)$$

To further evaluate the CAFE model, modeled NPP is compared to direct NPP measurements at the Hawaii Ocean and Bermuda Atlantic Time Series stations (HOT and BATS) for the period 2003–2014. Unlike the PPARR validation above, in this analysis the CAFE model uses 8 day satellite composites averaged across a 27 × 27 km grid around each station, as well as direct conductivity-temperature-depth (CTD) measurements

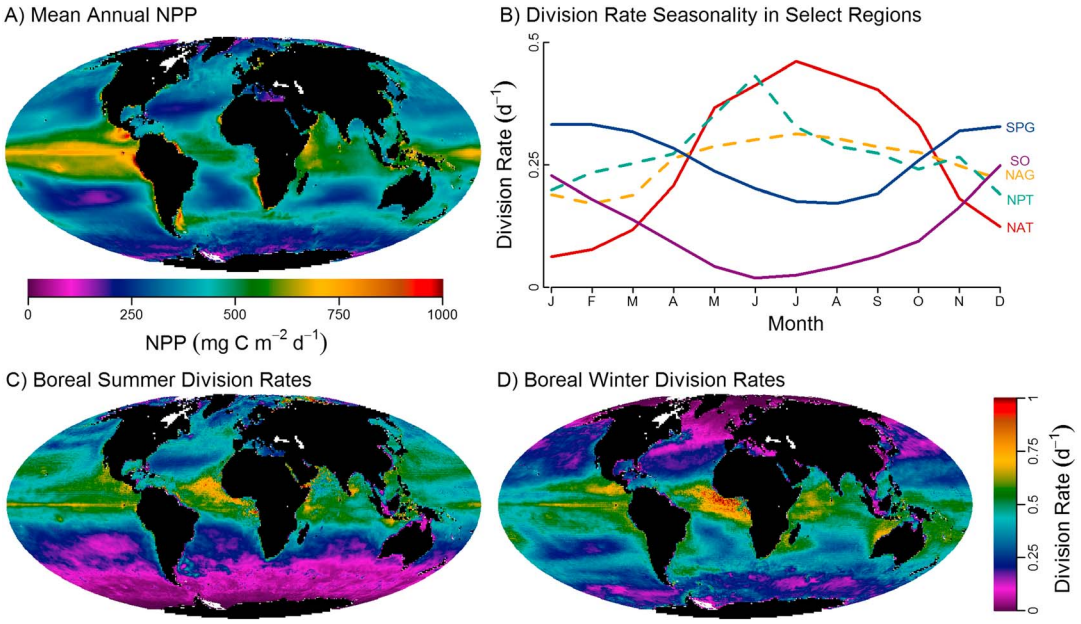

Figure 3. Global CAFE model climatology showing (a) mean annual NPP and (b) phytoplankton division rates in the surface mixed layer for the five oceanic regions delineated in Figure 2. Phytoplankton division rates in the surface mixed layer during the (c) boreal summer and (d) boreal winter.

to compute MLD. Subsequent 8 day CAFE time series at each station are linearly interpolated to the monthly HOT and BATS NPP time series. This approach is repeated for the VGPM, AM96, and CbPM models, and each model is evaluated using the test statistics above (equations 22–24).

3. Data

The reassessment of global NPP, model comparisons and sensitivity analyses are all populated using monthly climatology Moderate Resolution Imaging Spectroradiometer (MODIS) Aqua L3 products (http://oceancolor.gsfc.nasa.gov/) averaged over the period 2003–2014. As listed in Table 1, the CAFE model uses five GIOP-DC IOPs (a_ϕ(443 nm), a_{dg}(443 nm), b_{bp}(443 nm), S_{dg}, and η), Chl *a*, PAR, and SST. Missing IOP and Chl *a* data for a given cell are linearly interpolated between months, while day length is also factored into the interpolation of missing PAR data. Global monthly climatological MLD data were derived by averaging monthly MLD data for the period 2003–2014 using gridded data from the NASA supported ocean productivity website (http://www.science.oregonstate.edu/ocean.productivity/). By necessity MLD climatology data blends different data sources (Simple Ocean Data Assimilation (SODA) model 2003–2004, Fleet Numerical Meteorology and Oceanographic Center (FNMOC) model 2005–2007, and Hybrid Coordinate Ocean Model (HYCOM) 2008–2014), and in each data source MLD is defined as the depth where the density of water is 0.125 kg m^{-3} greater than the density at a reference depth of 10 m [*Levitus*, 1982]. As the SODA MLD data have a spatial resolution of 1°, all global input fields were averaged into 1° spatial bins for input into the CAFE model. Finally, 8 day satellite composites at the HOT and BATS sites are also MODIS Aqua L3 products. CTD data used to compute MLD at HOT and BATS are from http://hahana.soest.hawaii.edu/hot/hot-dogs/ and http://bats.bios.edu/, respectively.

4. Results and Discussion

4.1. Model Climatology

Global climatological patterns of NPP and phytoplankton division rates ($d = \mu/\log(2)$) from the CAFE model are presented in Figure 3. NPP rates are areally integrated through the euphotic zone, while division rates correspond to phytoplankton in the surface mixed layer only. Global oceanic NPP from the CAFE model (52 Pg C m^{-2} yr^{-1}) is slightly higher than the frequently cited 50 Pg C m^{-2} yr^{-1} [*IPCC*, 2013]. NPP is highest in regions of equatorial divergence and coastal upwelling sites and lowest in the South Pacific subtropical gyre, eastern Mediterranean Sea, and polar waters (Figure 3a). Globally averaged phytoplankton division

Table 2. Sensitivity Analysis of Parameters within the CAFE Model Framework[a]

Model Run Description	Global NPP (Pg C yr^{-1})	Latitudinal NPP (Pg C yr^{-1})					
		90°N–60°N	60°N–30°N	30°N–0°	0°–30°S	30°S–60°S	60°S–90°S
CAFE default configuration	52.15	1.38	5.98	15.21	16.75	11.26	1.58
Sensitivity Analyses		Fraction of CAFE Default Configuration					
PAR calculated from *Bricaud et al.* [1998]	54.60	0.88	1.08	1.09	1.05	1.00	0.94
$a_\phi(\lambda) + (\phi_\mu)$ uncertainty (GIOP-DC)	56.96	1.13	1.13	1.10	1.08	1.07	1.06
$E_K - a_\phi$ uncertainty (GIOP-DC)	46.43	0.73	0.85	0.88	0.91	0.92	0.91
SST derived from SST	51.04	0.59	0.95	1.03	1.06	0.89	0.59
Current E_K parameterization + 10%	55.80	1.07	1.07	1.07	1.07	1.07	1.07
Current E_K parameterization − 10%	48.50	0.94	0.93	0.93	0.93	0.93	0.94
No increases in subsurface $a_\phi(\lambda)$	47.98	0.97	0.93	0.90	0.90	0.96	0.98
Subsurface $a_\phi(\lambda)$ doubles	55.33	1.03	1.05	1.08	1.07	1.03	1.02

[a]The top row summarizes global and latitudinal annual NPP for the default configuration of the CAFE model. Subsequent rows describe the sensitivity analysis performed, resultant global NPP, and the fractional change in latitudinal regions relative to the default configuration of the CAFE model.

rates are 0.34 day^{-1}, which correspond to a doubling time of approximately 3 days. For reference, the global average is slightly higher than the annual means of the five regions shown in Figure 3b where, excluding the Southern Ocean (0.11 day^{-1}), annual average division rates varied between 0.25 and 0.28 d^{-1}. The North Atlantic has the most pronounced seasonality where division rates ranges from 0.06 day^{-1} in January to 0.46 day^{-1} in July. The seasonal range in the North Pacific is comparatively muted, ranging from 0.19 d^{-1} in December to 0.43 d^{-1} in June. The higher winter rates in the North Pacific are driven largely by shallower mixed layer depths (MLD ≈ 100 m) that enable phytoplankton to absorb more light than the deeper mixing North Atlantic (winter MLD > 200 m) [*Westberry et al.*, 2016]. That the annually averaged division rates in the South Pacific and North Atlantic Gyres are similar to the higher latitude regions may seem surprising given these gyres have persistently low Chl *a* concentrations. Low winter division rates in the higher latitude regions are certainly a dominant mechanism driving this annual convergence. However, the subsequent discussion also demonstrates that the productivity of subtropical gyres is likely higher than previously predicted by other widely cited models. In the following sections the individual components of the CAFE model are described and validated. Next, a comparison of the CAFE and 21 other models to direct NPP measurements shows the CAFE model yields the most accurate satellite-based NPP estimates. Having established the accuracy and mechanistic structure of the CAFE model, the final section returns to global NPP estimates and provides a more detailed comparison to other widely cited models.

4.2. Model Parameterization

This section is divided into three subsections that describe the structure of the CAFE model, and how and why it differs from previously published absorption-based models. The first subsection describes the absorption of energy by phytoplankton, followed by a description of how photoacclimation dictates the partitioning of absorbed energy between photochemical and nonphotochemical sinks, and finally an overview of the conversion of photochemically absorbed energy into carbon biomass. Model sensitivity analyses are discussed in each subsection and summarized in Table 2.

4.2.1. Absorbed Energy

Spectral inversion algorithms now permit the derivation of phytoplankton absorption coefficients (a_ϕ) and other inherent optical properties (IOPs) from satellite ocean color data [*Lee et al.*, 2002; *Maritorena et al.*, 2002; *Werdell et al.*, 2013]. The CAFE model is one of a few absorption-based models that directly exploits spectral inversion algorithms [*Lee et al.*, 2011; *Z. Lee et al.*, 2015; *Kahru et al.*, 2015], as most other published models derive E_K as the product of Chl *a* and an assumed Chl *a*-normalized absorption coefficient $\left(a^*_\phi\right)$. In the models of *Smyth et al.* [2005] and *Ondrusek et al.* [2001], a^*_ϕ is constant. In the model of *Marra et al.* [2003], a^*_ϕ varies with sea surface temperature with higher values predicted in warmer waters. In the model of AM96, a^*_ϕ is not directly computed but rather the product $a^*_\phi \times \phi^{\max}_\mu$ is assumed constant.

The CAFE model employs the GIOP-DC algorithm as it had the most accurate $a_\phi(\lambda)$ retrievals amongst currently available inversion algorithms when evaluated against in situ measurements within the NASA

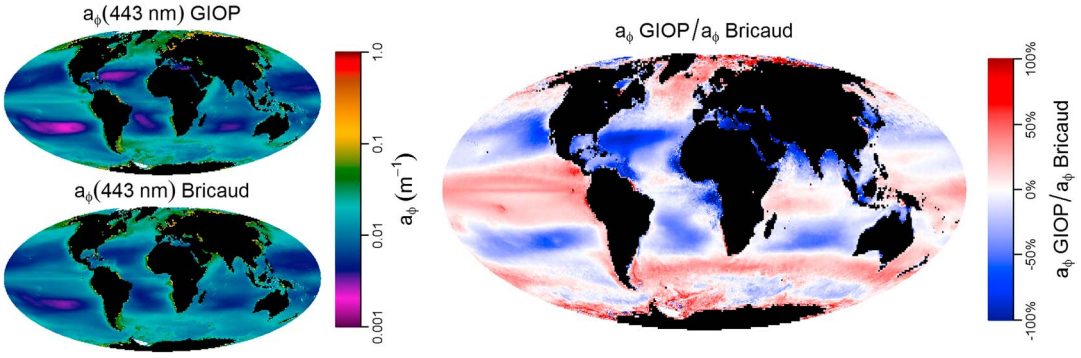

Figure 4. Annual climatology of a_ϕ(443 nm) computed from the GIOP-DC and estimated empirically as function of Chl *a* following *Bricaud et al.* [1998], and the percent difference between the two approaches.

bio-optical marine algorithm data set [*Brewin et al.*, 2015]. A series of manuscripts by *Bricaud et al.* [1995, 1998, 2004] have analyzed a_ϕ variability in the global ocean and are used here to qualitatively evaluate the GIOP-DC. *Bricaud et al.* [1995, 1998] document that Chl *a* explains greater than 60% of $a_\phi(\lambda)$ variance. Their analysis shows that as Chl *a* increases (1) a^*_ϕ decreases and (2) the spectral shape of $a_\phi(\lambda)$ shifts toward increased relative absorption in the longer (>550 nm) wavelengths. As noted in section 4.2, the magnitude of $a_\phi(\lambda)$ is unconstrained in the GIOP-DC algorithm (i.e., it is not directly tied to Chl *a*), but its spectral shape is defined by the Chl *a*-dependent coefficients presented in *Bricaud et al.* [1998]. Figure 4 compares global annual patterns of a_ϕ(443 nm) derived from the GIOP-DC and a_ϕ(443 nm) calculated from Chl *a* (OCI algorithm [*Hu et al.*, 2012]) following *Bricaud et al.* [1998]. The two approaches show very similar global patterns and linearly covary ($r^2 = 0.67$, $p < 0.001$, $n = 5{,}675{,}259$). However, significant differences exist across much of the ocean when viewed by the percent difference between the two approaches (Figure 4). In the subtropical gyres, a_ϕ from the GIOP-DC is approximately 50% lower than a_ϕ computed from Chl *a*, while in temperate and equatorial waters a_ϕ from the GIOP-DC is approximately 50% higher. The largest source of variance in the Chl *a* versus $a^*_\phi(\lambda)$ relationship is cell size [*Bricaud et al.*, 2004], such that at a given Chl *a* concentration, large phytoplankton cells absorb more energy than small phytoplankton cells (i.e., a^*_ϕ is higher in microplankton than picoplankton at equivalent Chl *a* concentrations). Consistent with the departure between Chl *a* and GIOP-DC estimates of a_ϕ (Figure 4), microplankton are increasingly dominant in temperate and upwelling waters, while picoplankton dominate biomass in subtropical gyres [*Brewin et al.*, 2010; *Marañón et al.*, 2012]. Thus, discrepancies between the two approaches are consistent with global patterns in phytoplankton size, which in turn lends increased confidence to employing the GIOP-DC estimates of ϕ_μ^{max} to derive absorbed energy.

Table 2 summarizes the CAFE model's sensitivity to measurements of $a_\phi(\lambda)$. Three CAFE model runs were performed where $a_\phi(\lambda)$ was calculated from Chl *a* (OCI algorithm) following *Bricaud et al.* [1998] and $a_\phi(\lambda)$ was calculated $\pm$ the uncertainty in GIOP-DC derived $a_\phi(\lambda)$ values. First, deriving $a_\phi(\lambda)$ from Chl *a* [*Bricaud et al.*, 1998] increased global NPP by 2.45 Pg C yr^{-1}. Consistent with Figure 4, NPP declined in polar waters and increased in subtropical and tropical waters where picophytoplankton are dominant. GIOP-DC-derived uncertainty in $a_\phi(\lambda)$ values has a larger influence on NPP, where addition and subtraction of uncertainty to $a_\phi(\lambda)$ increased and decreased global NPP by 4.8 and 5.7 Pg C yr^{-1}, respectively. Global NPP is more sensitive to an equivalent decrease in $a_\phi(\lambda)$ (relative to an equivalent increase) simply because $a_\phi(\lambda)$ is a small fraction of total absorption (equation (7)). A detailed spatial analysis of $a_\phi(\lambda)$ uncertainty is beyond the scope of this research, though Table 2 does show that global NPP is most sensitive to $a_\phi(\lambda)$ uncertainty in temperate and polar waters in the Northern Hemisphere.

Planned hyperspectral satellite sensors (e.g., NASA's PACE instrument) may afford more accurate measurements of $a_\phi(\lambda)$ from space. In general, the accuracy of such retrievals increases with higher spectral resolution by relaxing the number of assumptions required when transforming water leaving radiance to inherent optical properties [*Werdell et al.*, 2013]. In particular, with hyperspectral data the GIOP-DC algorithm may not need to anchor the spectral shape of $a_\phi(\lambda)$ to Chl *a*. Unconstrained spectral assessments of $a_\phi(\lambda)$ could improve the derivation of absorbed energy but perhaps more importantly could allow scientists to track broad changes in

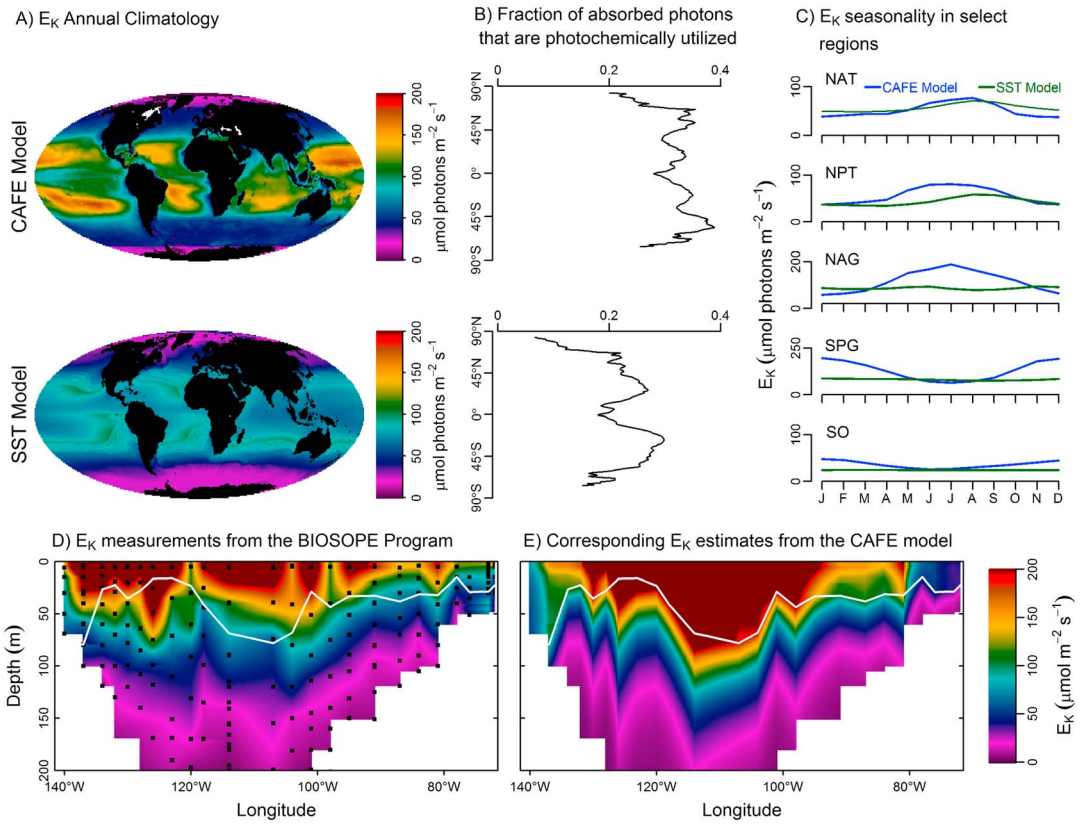

Figure 5. (a) The annual climatology of E_K modeled as a function of the optical environment (top) and a function of sea surface temperature (bottom). (b) The corresponding fraction of absorbed energy dissipated as NPQ predicted by each model, averaged by latitude. (c) Monthly climatology of E_K for the two models in five regions delineated in Figure 2. All data in Figures 5a–5c corresponds to the surface mixed layer only, and the optical model has been spectrally scaled to match the SST model. (d) E_K measurements from the South Pacific [*Huot et al.*, 2008] are shown against (e) the corresponding E_K values derived from the optical model.

phytoplankton taxa (at the pigment level) through space and time. The Hyperspectral Imager for the Coastal Ocean was recently used to discern a toxic phytoplankton bloom by identifying its unique fluorescence signature that could not otherwise be captured with extant multispectral satellite platforms [*Dierssen et al.*, 2015].

4.2.2. Photoacclimation (E_K)

E_K represents a key phytoplankton physiological property in productivity models, as it defines whether absorbed energy is used to fuel growth or is dissipated as heat or fluorescence. As ϕ_μ^{max} is largely constrained across the global ocean (next section), E_K drives much of the global variability in ϕ_μ and is consequently paramount to generating accurate estimates of μ and NPP. The parameterization of ϕ_μ^{max} varies widely across NPP models. The absorption-based model of *Marra et al.* [2003] assumes that ϕ_μ^{max} is globally constant at 116 μmol m^{-2} s^{-1}. In contrast, *Ondrusek et al.* [2001] varies E_K as a function of PAR, such that PAR values of 10 and 1500 μmol m^{-2} s^{-1} correspond to F_V/F_M values of 35 and 105 μmol m^{-2} s^{-1}, respectively. The models AM96 and *Smyth et al.* [2005] employ identical models for F_V/F_M and describe it as a function SST following *Morel et al.* [1996], where SSTs of 5°C and 25°C yield ϕ_μ^{max} values of 31 and 110 μmol photons m^{-2} s^{-1}, respectively.

The CAFE model adopts the new ϕ_μ^{max} model of *Behrenfeld et al.* [2016], which is based on fundamental principles of chlorophyll synthesis regulation. A comparison of the global annual climatology of ϕ_μ^{max} employed by the CAFE model and the SST-based ϕ_μ^{max} values from *Morel et al.* [1996] is shown in Figure 5a. While both models predict that ϕ_μ^{max} declines poleward, the CAFE model predicts significantly higher values in the stratified subtropical oceans and lower values in upwelling coastal zones. These differences in ϕ_μ^{max} translate to

large differences in the calculated amount of absorbed energy passed to the photosynthetic reaction centers (Figure 5b). Both models predict that a greater fraction of absorbed energy is dissipated as NPQ in polar versus subtropical waters, which is consistent with field data [*Browning et al.*, 2014]. However, the CAFE model predicts that approximately 35% of absorbed photons drive photochemistry in subtropical waters, compared to ~25% predicted by the SST model. The annual averages shown in Figures 5a and 5b mask the large seasonal differences between these two approaches. Across the five regions delineated in Figure 2, the new model predicts much greater seasonality in ϕ_μ^{max} relative to the SST model (Figure 5c), particularly in subtropical waters. For example, the annual ϕ_μ^{max} range in the North Atlantic is slightly larger in the CAFE model (38–77 $\mu mol\, m^{-2}\, s^{-1}$) relative to the SST model (49–71 $\mu mol\, m^{-2}\, s^{-1}$), reflecting similar annual ranges in mixed layer water temperature and optical environment. In the South Pacific Gyre, however, the annual ϕ_μ^{max} range predicted by the CAFE model (65–196 $\mu mol\, m^{-2}\, s^{-1}$) is much greater than the range in the SST model (76–86 $\mu mol\, m^{-2}\, s^{-1}$). In this region, the mixed layer optical environment is variable through the year despite small changes in SST. Sensitivity analyses are shown in Table 2. When the CAFE model was run with SST-based ϕ_μ^{max} estimates, global NPP declined 1.11 Pg C yr^{-1}. The analysis in Figures 5a–5c and discussed above pertains to ϕ_μ^{max} in the surface mixed layer only. A second major difference in ϕ_μ^{max} models is that the CAFE model is the only model that allows ϕ_μ^{max} to vary beneath the mixed layer, all other models assume vertical homogeneity. The importance of this assumption can be inferred from Table 2, where implementation of SST-based ϕ_μ^{max} estimates actually increases NPP in stratified subtropical and tropical waters despite lower surface values. Table 2 also documents changes in NPP assuming a 10% error in the new ϕ_μ^{max} model of *Behrenfeld et al.* [2016] adopted here. Increases and decreases in ϕ_μ^{max} by 10% both increase and decrease global NPP by 3.65 Pg C yr^{-1}, and the fractional changes in latitude are spatially muted.

The photoacclimation model of *Behrenfeld et al.* [2016] was originally evaluated against field data from HOT, BATS, and the Atlantic Meridional Transect (AMT) field programs. Here we further evaluate this new ϕ_μ^{max} model by comparison with the field data reported by *Huot et al.* [2008] from the BIOSOPE (Blogeochemistry and Optics South Pacific Experiment) program. Depth-resolved measurements span different trophic regimes from the eutrophic upwelling region of the Chilean coast to the mesotrophic area associated with the plume of the Marquieses Islands in the high-nutrient low-chlorophyll (HNLC) subequatorial waters and to the extremely oligotrophic South Pacific Gyre [*Claustre et al.*, 2008]. Figures 5d and 5e shows longitudinal and depth maps of measured and modeled ϕ_μ^{max}, respectively. These comparisons indicate a statistically significant linear relationship between modeled and measured ϕ_μ^{max} ($r^2 = 0.64$, $n = 143$, $p < 0.01$), with an intercept not significantly different than 0, and a slope of 0.98. One clear discrepancy between the measured and modeled ϕ_μ^{max} shown in Figures 5d and 5e is that the BIOSOPE data show vertical structure within the mixed layer, whereas the CAFE model implicitly assumes homogeneity within the MLD (though some vertical heterogeneity is introduced through changes in the spectral quality of light through depth). In the CAFE model the MLD is delineated as the depth where the density of water exceeds 0.125 kg m^{-3} the density at a reference depth of 10 m [*Levitus*, 1982], which is greater than the more widely used 0.03 kg m^{-3} threshold [e.g., *de Boyer Montégut et al.*, 2004]. Substituting the 0.03 kg m^{-3} threshold into the BIOSOPE data yields an approximate twofold shallower MLD and in turn increases the linear relationship between the measured and modeled ϕ_μ^{max} ($r^2 = 0.71$, $n = 143$, $p < 0.01$). The broad ϕ_μ^{max} patterns shown in the BIOSOPE data are also consistent with a depth-resolved data set from the northeast tropical Atlantic Ocean [*Babin et al.*, 1996]. This data set also shows that despite a modest range is SST (18°C to 24°C), ϕ_μ^{max} within the surface mixed layer decreased from 400 $\mu mol\, m^{-2}\, s^{-1}$ in oligotrophic waters to ~160 $\mu mol\, m^{-2}\, s^{-1}$ in eutrophic waters. Consistent with the BIOSOPE data and our parameterization, ϕ_μ^{max} also decreased beneath the MLD and reached a minima near the euphotic depth.

4.2.3. Quantum Efficiency of Growth $\left(\phi_\mu^{\max}\right)$

In the present model, we assumed $\left(\phi_\mu^{\max}\right)$ varies between 0.018 to 0.030 mol C (mol photons)$^{-1}$ in high- and low-light environments, respectively. This parameterization is based on the observation in field data sets that E_K positively covaries with the relative magnitude of nonphotosynthetic pigments and negatively covaries with $\phi_\mu^{\max}$ [*Uitz et al.*, 2008]. Our parameterization of $\phi_\mu^{\max}$ is lower than most previously published models, where the treatment of $\phi_\mu^{\max}$ can vary widely. In this section we review how various models estimate $\phi_\mu^{\max}$

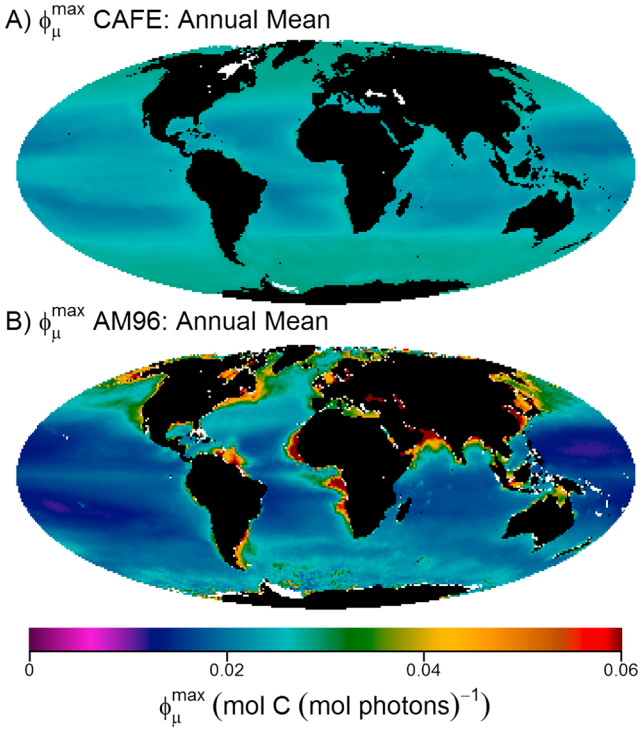

Figure 6. A comparison of mean annual φ_μ^{max} estimates from (a) the CAFE and (b) AM96 models.

and then highlight how our treatment is consistent with field and culture measurements, as well as an a priori estimate based on the energetic stoichiometry of phytoplankton.

Several NPP models assume ϕ_μ^{max} is globally constant, but the ascribed value varies twofold between these models (0.030 mol C (mol photons)$^{-1}$ in *Ondrusek et al.* [2001] and 0.060 mol C (mol photons)$^{-1}$ in *Smyth et al.* [2005] and *Marra et al.* [2003]). *Uitz et al.* [2008] parameterized ϕ_μ^{max} through an analysis of in situ data, yielding lowest values in stratified, high-light surface waters and highest values in low-light environments (e.g., beneath the surface mixed layer or in regions where mixing extends beneath the euphotic depth), which is consistent with our approach here. It should be noted, however, that the field data used in their model were derived from short-term (1–4 h) ^{14}C incubations, which measure an intermediate quantity between gross and net production and thus likely overestimate ϕ_μ^{max} [*Halsey et al.*, 2010, 2011]. Finally, AM96 predict ϕ_μ^{max} to vary in space and time but assume the product $a_\phi^* \times \phi_\mu^{max}$ is constant (i.e., $\alpha^B = 16$ g C (g chl)$^{-1}$ (mol photons m^{-2})$^{-1}$). Annually averaged ϕ_μ^{max} for the CAFE and AM96 models are shown in Figure 6. The CAFE model predicts that ϕ_μ^{max} has a mean ± standard deviation of 0.025 ± 0.002 mol C (mol photons)$^{-1}$, compared to 0.023 ± 0.009 mol C (mol photons)$^{-1}$ for AM96. While these overall averages are similar, AM96 predicts greater spatial variability with values greater than 0.060 mol C (mol photons)$^{-1}$ in coastal and upwelling regions. To our knowledge, the only comprehensive field ϕ_μ^{max} data sets using 24 h incubations are from *Wozniak et al.* [1992] and *Marra et al.* [2007]. In these studies, ϕ_μ^{max} exhibits a constrained range within their respective areas of study, with values of 0.018, 0.020, 0.020, 0.030, and 0.030 mol C (mol photons)$^{-1}$ for the temperate Atlantic Ocean, Ross Sea, Arabian Sea, Black Sea, and Baltic Sea, respectively. The CAFE model predicts strikingly similar ϕ_μ^{max} values of 0.020, 0.027, 0.021, 0.024, and 0.027 mol C (mol photons)$^{-1}$ in these five respective regions.

The quantum efficiency of growth has also been extensively measured in steady state cultures (Table 3). Unfortunately, the photoacclimation state of these cultures (i.e., $a_\phi(\lambda)$) is not always stated and it is therefore not possible to derive ϕ_μ^{max} from all the tabulated ϕ_μ measurements. Nevertheless, it appears that E_K is largely invariant across nutrient-limited growth rates [*Behrenfeld et al.*, 2004; *Halsey et al.*, 2010] and is generally a factor of 0.5 to 0.75 lower than the growth irradiance [*Geider et al.*, 1998; *Halsey et al.*, 2010]. Across all taxa and division rates listed in Table 3, ϕ_μ has a mean ± standard deviation of 0.016 ± 0.005 mol C (mol photons)$^{-1}$. If we assume that $E_K = E_G \times 0.75$ within the expression $\tanh(E_K/E_G)$, then these data give a mean ± standard deviation for ϕ_μ^{max} of 0.025 ± 0.008 mol C (mol photons)$^{-1}$, which is consistent with the CAFE model.

The energetic stoichiometry of phytoplankton can also be used to generate a priori estimates of ϕ_μ^{max}. The theoretical upper limit of ϕ_μ^{max} is commonly cited as 0.125 mol C (mol photons)$^{-1}$. This value represents optimal coupling of linear photosynthetic electron transport with Calvin cycle activity, where 24 mol of absorbed photons yield the precise amount of energy and reductant to reduce 1 mol of glyceraldehyde-3-phosphate (G3P). However, this optimal efficiency does not account for the various potential fates of absorbed light energy. When all photosynthetic reaction centers are oxidized (i.e., subsaturating irradiance), a significant

Table 3. Culture Measurements of φ_μ Across Nutrient-Limiting Growth Rates

Limiting Resource	Species	E_G	C:Chl	μ	φ_μ
		Laws and Bannister [1980]			
NO_3	*T. weissflogii*	247	336	0.15	0.011
NO_3	*T. weissflogii*	241	144	0.34	0.017
NO_3	*T. weissflogii*	239	111	0.48	0.019
NO_3	*T. weissflogii*	236	95	0.72	0.022
NO_3	*T. weissflogii*	233	62	0.94	0.021
NH_4	*T. weissflogii*	246	218	0.17	0.015
NH_4	*T. weissflogii*	244	185	0.30	0.018
NH_4	*T. weissflogii*	240	133	0.05	0.022
NH_4	*T. weissflogii*	235	96	0.68	0.021
NH_4	*T. weissflogii*	231	69	0.94	0.022
PO_4	*T. weissflogii*	236	223	0.18	0.013
PO_4	*T. weissflogii*	231	195	0.27	0.017
PO_4	*T. weissflogii*	230	128	0.47	0.020
PO_4	*T. weissflogii*	224	101	0.66	0.023
PO_4	*T. weissflogii*	221	63	0.92	0.022
		Jakob et al. [2007]			
NO_3	*P. tricornutum*	168	85	0.07	0.006
NO_3	*P. tricornutum*	36	25	0.11	0.009
		Halsey et al. [2010]			
NO_3	*D. tertiolecta*	235		0.45	0.014
NO_3	*D. tertiolecta*	235		0.85	0.013
NO_3	*D. tertiolecta*	235		1.53	0.016
NO_3	*T. weissflogii*	235	303	0.2	0.014
NO_3	*T. weissflogii*	235	93	0.5	0.014
NO_3	*T. weissflogii*	235	42	1.0	0.014
		Halsey et al. [2014]			
NO_3	*O. tauri*	205	63	0.2	0.014
NO_3	*O. tauri*	205	64	0.5	0.014
NO_3	*O. tauri*	205	53	1.0	0.018
NO_3	*M. pusilla*	205	149	0.2	0.003
NO_3	*M. pusilla*	205	102	0.5	0.005
NO_3	*M. pusilla*	205	118	1.0	0.016

fraction of absorbed energy is dissipated as heat or re-emitted as fluorescence [*Huot and Babin*, 2010]. Critically, this loss of absorbed energy is independent of additional light-dependent losses (as dictated by E_K) and must therefore be accounted for by lowering $\phi_\mu^{\max}$. The degree in which $\phi_\mu^{\max}$ is lowered can be estimated from low-light measurements of the quantum efficiency of photosystem II (i.e., F_V/F_M). In cultures and in situ, F_V/F_M generally falls between 0.50 to 0.60 in the absence of nonphotochemical quenching [*Behrenfeld et al.*, 2006; *Suggett et al.*, 2009]. These values imply a 40–50% light-independent loss of absorbed energy [*Huot and Babin*, 2010]. Thus, in the context of absorption-based models, a $\phi_\mu^{\max}$ of 0.075 mol C (mol photons)$^{-1}$ is a more realistic upper limit. This upper limit represents gross primary production (GPP), where all absorbed photons yield the precise energy and reductant to convert CO_2 to G3P. The energetic stoichiometry of phytoplankton growth and NPP must also account for all catabolic processes that respire fixed carbon back to CO_2 and all anabolic processes that divert photosynthetic energy and reductant away from the Calvin cycle [*Behrenfeld et al.*, 2004, 2008]. Over a diel cycle, these processes further lower $\phi_\mu^{\max}$ by a magnitude that can be estimated as the ratio of GPP to NPP. A comprehensive comparison of paired GPP (^{18}O technique) and NPP measurements collected during the Joint Global Ocean Flux Study program yields a robust GPP:NPP ratio of 2.7 [*Hendricks et al.*, 2005; *Marra*, 2002]. Steady state monoculture experiments spanning a large range of growth rates indicate a GPP:NPP ratio of 3.3 [*Halsey and Jones*, 2015]. Dividing 0.075 mol C (mol photons)$^{-1}$ by these field and culture-based GPP:NPP ratios gives $\phi_\mu^{\max}$ values of 0.030 and 0.022 mol C (mol photons)$^{-1}$, respectively, that again are bracketed by CAFE model estimates.

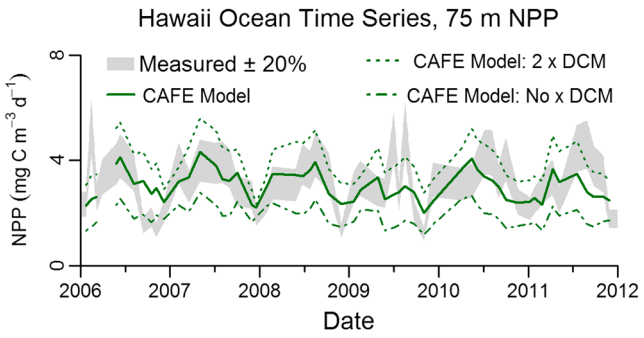

Figure 7. Measured and modeled NPP beneath the mixed layer (75 m) at the Hawaii Ocean Time Series. The grey shaded area represents an assumed 20% measurement error in direct NPP measurements. The solid green line is the default configuration of the CAFE model. The dotted line is the CAFE model where depth-dependent increases in a are doubled, and the dash-dotted lined is the CAFE model where (C_{Phyto}) is equivalent to surface values.

4.2.4. Subsurface Productivity

Phytoplankton properties derived from satellite ocean color data correspond to natural communities within the surface mixed layer. In most of the global ocean, sufficient light passes through the surface mixed layer to enable phytoplankton growth at depths hidden from satellite detection [*Silsbe and Malkin*, 2016]. In these darker waters, light limitation elicits genotypic (photo-adaptation) and phenotypic (photoacclimation) responses in phytoplankton communities that are often observed as subsurface chlorophyll maximum layers (SCMLs). Specific mechanisms regulating community composition, distribution, and productivity in SCMLs are variable through space and time (reviewed in *Cullen* [2015]). In the most oligotrophic and clearest waters, elevated chlorophyll at the SCML almost entirely reflects a photoacclimation response, with no matching increases in phytoplankton biomass at depth [*Mignot et al*., 2014; *Cullen*, 2015]. In stratified waters that support a higher flux of nutrients, SCMLs are promoted at shallower optical depths (i.e., depths with higher light climate) [*Uitz et al*., 2006], and the increase in Chl *a* observed at the SCML is progressively more associated with an increase in phytoplankton biomass [*Cullen*, 2015].

The treatment of subsurface biomass and productivity varies across satellite-based models. Some models assume all input parameters (e.g., a_ϕ, E_K, and ϕ_μ^{max}) are invariant with depth [*Smyth et al*., 2005; *Marra et al*., 2003], while other models recognize that the distinct phytoplankton physiology in subsurface communities demands a depth explicit approach [e.g., *Westberry et al*., 2008]. Syntheses of large data sets have yielded empirical equations that predict depth-dependent increases in Chl *a* relative to surface concentrations [e.g., *Morel and Berthon,* 1989; *Uitz et al.,* 2006]. Two absorption-based models (AM96 [*Ondrusek et al.,* 2001]) have applied these empirical equations to model the vertical distribution of a_ϕ through the euphotic zone. The CAFE model predicts that E_K decreases beneath the mixed layer and that as E_K declines, a_ϕ increases (equation (18)). Consistent with predicted depth-dependent increases in Chl *a* [*Uitz et al*., 2006], the CAFE model predicts that depth-dependent a_ϕ increases are maximal in stratified oligotrophic waters and minimal in eutrophic waters (data not shown).

Two sensitivity analyses document the influence of the vertical distribution of a_ϕ on global NPP (Table 2). If the CAFE model is run such that a_ϕ was constant through the euphotic depth, global NPP declines by 4.17 Pg C yr^{-1} with the most pronounced changes in the permanently stratified tropical waters. If the CAFE model is run such that depth-dependent increases in a_ϕ were doubled, global NPP increases by 3.18 Pg C yr^{-1} with the greatest increases again in the permanently stratified tropical waters. The default configuration of the CAFE model alongside these two alternate $a_\phi(z)$ parameterizations was also applied to MODIS Aqua data at the Hawaiian Ocean Time Series. Figure 7 illustrates resultant volumetric rates of NPP from the three model runs alongside in situ NPP measurements at 75 m (i.e., beneath the mixed layer for 93% of data). The default configuration of $a_\phi(z)$ in the CAFE model (equation (18)) yielded a very small bias (−0.006) when compared to in situ measurements. Conversely, assuming a_ϕ is constant with depth underestimated NPP (bias = −0.213), while doubling depth-dependent increases in a_ϕ overestimated NPP (bias = 0.114). This exercise was repeated at 100 m and again the CAFE model bias (0.073) was lower than the other two scenarios (−0.178 and 0.192).

4.3. Model Validation

The CAFE model performed very well when evaluated alongside NPP field measurements. Figure 8a compares the CAFE model performance against the 21 other NPP models included in the *Saba et al.* [2011] data set where direct NPP measurements from all 10 regions are pooled together (Figure 2). Overall, the CAFE

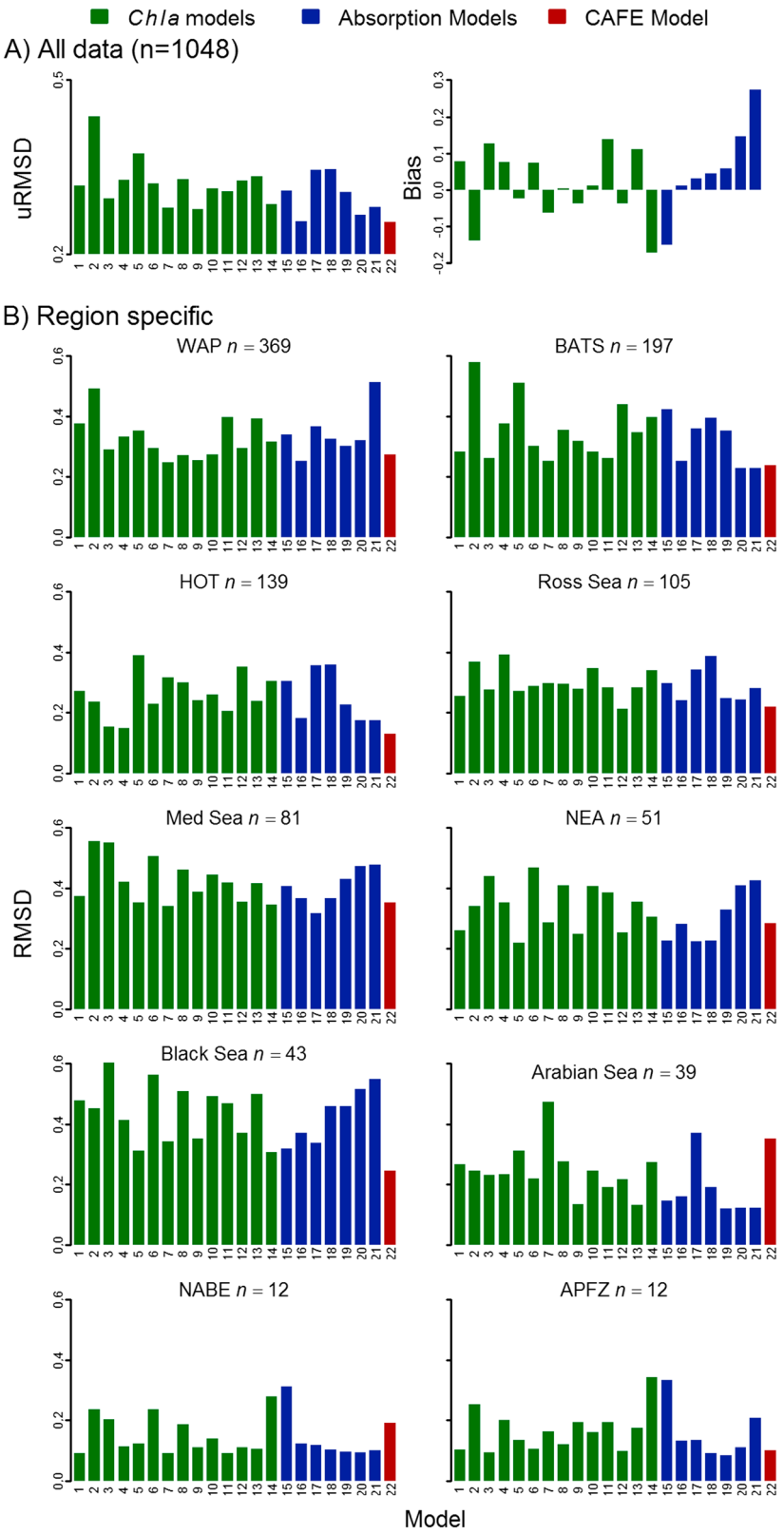

Figure 8. (a) NPP model skill partitioned into variance (uRMSD) and bias for all in situ data sets. Models 1–21 are previously published NPP models listed in *Saba et al.* [2011], green and blue models are Chl *a* and absorption-based models, respectively, and the CAFE model is shown in red. Note that the very low CAFE model bias is too small to see. (b) Region specific model skill (RMSD) separated into the 10 in situ data sets shown in Figure 2.

model explained both the greatest amount of variance (uRMSD = 0.255) and had the lowest absolute model bias (0.003, Figure 8a; note that the model bias is too low to be visible). Taken together, the CAFE model had the highest model skill (RMSD = 0.255) across the pooled data set, slightly better than the absorption-based model of *Antoine and Morel* [1996] (RMSD = 0.257).

CAFE model skill, like all models, varied between ocean regions (Figure 8b). The CAFE model performed better than average in 8 of the 10 regions and was the only model with lowest RMSD in more than one region (Hawaii Ocean Time Series (HOT), Black Sea). However, the model performed poorly in the Arabian Sea and North Atlantic Bloom Experiment (NABE) data sets. In these regions the CAFE model was effective at reproducing the variance of NPP measurements, as the uRMSD was 0.15 and 0.08 in Arabian Sea and NABE data sets, respectively. Poor model skill was instead driven by model bias, as the CAFE model underestimated NPP by factor of 1.97 and 1.48 in these two data sets, respectively. Mean calculated photosynthetic assimilation efficiencies (P^B_{Opt} [*Behrenfeld and Falkowski*, 1997]) were 8.4 and 3.4 mg C (mg Chl)$^{-1}$ h^{-1} in the Arabian Sea and NABE data sets, respectively. These assimilation efficiencies are within the range of measured values [*Behrenfeld and Falkowski*, 1997] and were also bracketed by higher and lower mean assimilation efficiencies at other regions where the CAFE model performed well (P^B_{Opt} = 1.5 and 11.2 mg C (mg Chl)$^{-1}$ h^{-1} at WAP and BATS, respectively). This suggests that the CAFE model is likely underestimating the total amount of energy absorbed (Q_{PAR}), rather than the conversion of absorbed energy into carbon biomass (ϕ_μ). Recall that with the PPARR approach, NPP models use tabulated in situ data rather than direct satellite measurements. As a result, the CAFE model estimated $a_\phi(\lambda)$ using Chl *a*-dependent coefficients [*Bricaud et al*., 1998] due to the absence of $a_\phi(\lambda)$ (and other IOP) measurements in the tabulated PPARR data set. Direct $a_\phi(\lambda)$ measurements from the Arabian Sea Joint Global Ocean Flux Study taken on a subset of stations clearly demonstrate that this approach underestimated $a_\phi(\lambda)$. Across eight stations where NPP was also measured, direct $a_\phi(\lambda)$ measurements from surface waters (filter pad technique) were on average 1.81 times greater than $a_\phi(\lambda)$ estimated from attendant Chl *a* measurements (high-performance liquid chromatography). Direct $a_\phi(\lambda)$ measurements are not available for the NABE data set; however NPP measurements coincided with the spring bloom that was dominated by diatoms and other large phytoplankton [*Lochte et al*., 1993]. Given that $a_\phi(\lambda)$ for larger microplankton typically exceed Chl *a*-based $a_\phi(\lambda)$ estimates [*Bricaud et al*., 2004], it is highly probable that Q_{PAR} is also underestimated in this particular data set. Indeed across the entire PPARR data set, estimating $a_\phi(\lambda)$ from Chl *a* likely diminished CAFE model skill. The ratio of $a_\phi(\lambda)$ from the GIOP-DC to that estimated using Chl *a* [*Bricaud et al*., 1998] was retrieved from monthly climatology data sets for each NPP measurement and compared to CAFE model bias. A statistically significant linear relationship ($p < 0.05$, $n = 1046$) confirms that locations where the CAFE model underestimated NPP coincides with regions where Chl *a*-based $a_\phi(\lambda)$ estimates are lower than $a_\phi(\lambda)$ from the GIOP-DC.

To further evaluate the CAFE model performance, we compared NPP estimates derived from satellite measurements to direct NPP measurements at the HOT and BATS sites. Results of this analysis are shown in Figure 9, alongside NPP calculated from the VGPM, AM96, and CbPM models. In Figure 10, the grey shaded area corresponds to an assumed 20% uncertainty around the direct NPP measurements [*Saba et al*., 2011]. Relative to using direct measurements as input (Figure 9b), running the CAFE model with satellite measurements improved model performance at HOT but lowered model performance at BATS. The RMSD at HOT and BATS for the satellite-based CAFE NPP data was 0.09 and 0.25, respectively (in contrast to RMSDs of 0.13 and 0.22 from tabulated in situ data). The RMSDs at HOT and BATS were 0.32 and 0.40 for the VGPM, 0.13 and 0.22 for AM96, and 0.15 and 0.40 for the CbPM, respectively. Thus, when combining both time series, the CAFE model had the highest model skill when run with satellite data. All four models were unable to reproduce the recurrent annual NPP maxima at BATS between January and March (Figure 9b). Unlike the Arabian Sea and NABE data sets discussed previously, this discrepancy appears to be largely driven by physiology rather than an underestimation of absorbed energy. A comparison of absorbed energy (equation (7)) calculated using satellite data against direct surface measurements of PAR, $a_\phi(\lambda)$, and $a_{\mathrm{dg}}(\lambda)$ collected between 2002 and 2011 (Bermuda Bio-Optics Project) showed strong linear covariance ($r^2 = 0.77$, $p < 0.01$, $n = 49$) where remotely sensed absorbed energy underestimated measured absorbed energy by a factor of only 0.94. Whether the discrepancy between the CAFE model and peak NPP at BATS is driven by photoacclimation (E_K) or the maximum quantum efficiency of growth, $\left(\phi_\mu^{\max}\right)$ is unclear and warrants further investigation.

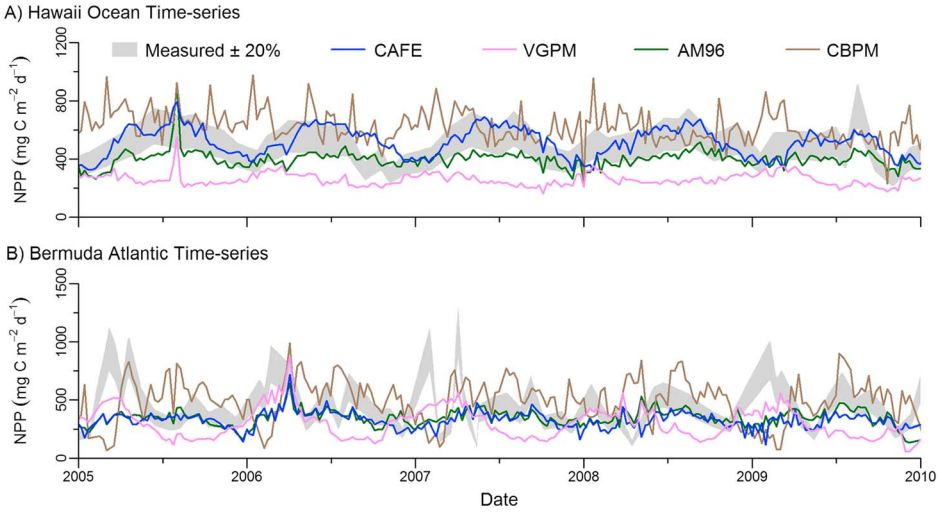

Figure 9. Direct NPP measurements from the (a) Hawaii Ocean and (b) Bermuda Atlantic Time Series are compared against satellite-derived estimates from CAFE, VGPM, AM96, and VGPM models. The grey shaded area represents an assumed 20% measurement error in direct NPP measurements.

4.4. Model Comparisons

Figure 10 compares NPP estimates from the CAFE model to the VGPM, CbPM, and AM96 models. Figure 10a shows the difference between annual NPP climatologies, and Figure 10b illustrates NPP monthly climatology for each model in the five oceanic regions delineated in Figure 2. Global annual NPP derived from AM96

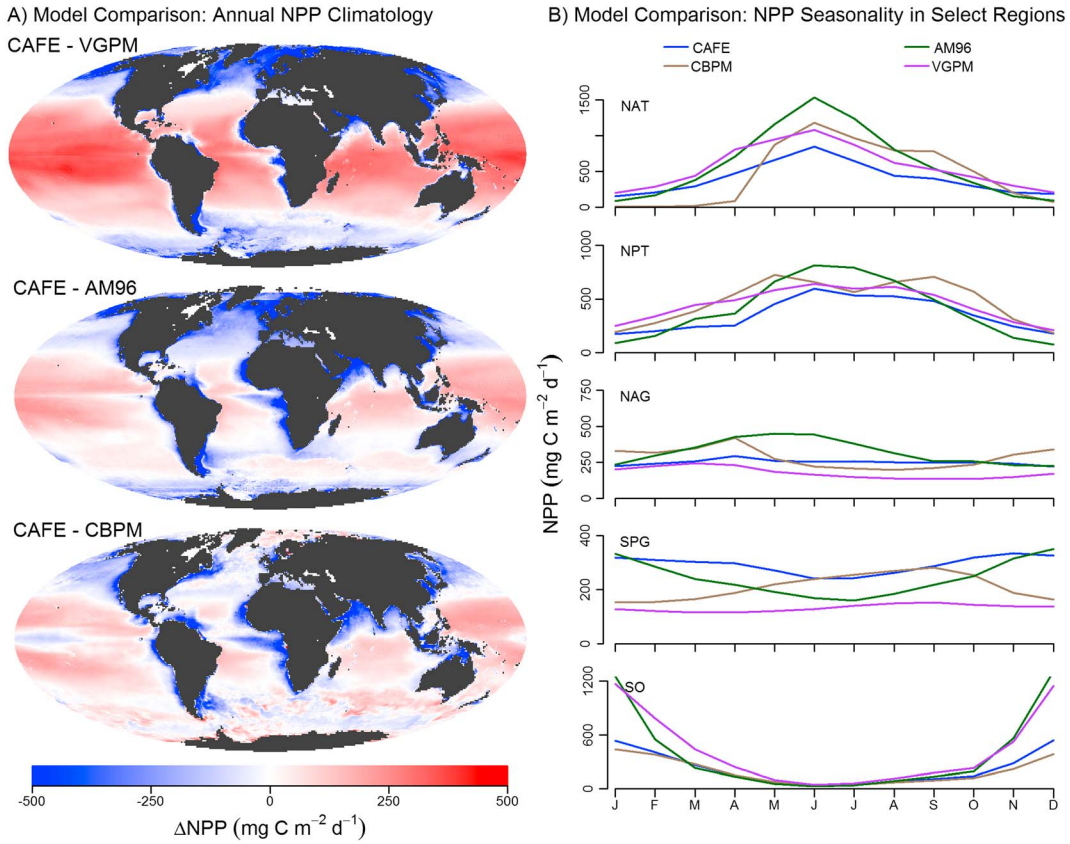

Figure 10. (a) Global patterns showing the difference between the CAFE model annual NPP climatology and three other models. (b) NPP monthly climatology for the five oceanic regions delineated in Figure 2 for the CAFE and three other models.

(60 Pg C yr^{-1}) exceeded the CAFE model (52 Pg C yr^{-1}), whereas global annual NPP derived from the CbPM (52 Pg C yr^{-1}) and VGPM (51 Pg C yr^{-1}) models was very proximal. Despite these similar global magnitudes, spatial disparities between NPP models are striking. The CAFE model predicts elevated NPP in tropical and subtropical waters and diminished NPP in temperate and polar waters relative to all other the models.

The exact mechanisms behind these large spatial disparities are model dependent, and given the different structure of each model (e.g., Chl *a* and carbon based), a comprehensive comparison is beyond the scope of this current research. Across all models, differences in the conversion of absorbed energy to carbon biomass is clearly a dominant factor behind the large spatial and temporal patterns shown in Figure 10. For example, in the VGPM, NPP is modeled as an asymptotic function of PAR (equation (19)). Consequently, the efficiency in which light is converted to carbon biomass is more than twofold greater when PAR is 20 mol photons m^{-2} d^{-1} relative to 45 mol photons m^{-2} d^{-1} (i.e., the proximate annual mean in temperate and tropical waters, respectively). In contrast, the CAFE model employs a new photoacclimation model based on fundamental principles of chlorophyll synthesis regulation [*Behrenfeld et al.*, 2016]. This well-validated component of the CAFE model (e.g., Figure 5) predicts latitudinal gradients of photochemical efficiency are relatively muted, which is consistent with field data [*Lin et al.*, 2016]. Spatial differences between the CAFE, AM96, and CbPM model are less pronounced. The AM96 model predicts that on average 50% more absorbed energy in the surface mixed layer is dissipated as nonphotochemical quenching than the CAFE model, and this difference approaches 100% in the subtropical gyres (Figure 5). While this disparity enhances CAFE model NPP in tropical and subtropical waters, it is partially mitigated as, unlike the CAFE model and field data [*Babin et al.*, 1996], AM96 assumes that E_K is constant through depth. In temperate and coastal regions NPP from AM96 exceeds CAFE model and this difference is largely driven by very high $\phi_\mu^{\max}$ (~0.06 mol C (mol absorbed photons)$^{-1}$) in the AM96 model. Annual global NPP climatology differences between the CAFE and CbPM models are broadly similar to the other models. Annual averages mask important differences in seasonality (Figure 10b). One dramatic difference in seasonality occurs in the South Pacific Gyre where the CAFE and AM96 models predict maximal NPP in the boreal winter, whereas the CbPM that predicts NPP is at its annual minima during this time. In this region NPP seasonality in the CAFE model is driven by Q_{PAR} which is maximal in December and January (3.54 mol photons d^{-1}) and minimal in June (1.90 mol photons d^{-1}). In contrast, seasonality in the CbPM is largely driven by satellite-detected Chl : C_{Phyto} that is maximal in July and minimal in December (0.004 and 0.002 mg Chl (mg C)$^{-1}$). In the CAFE model the efficiency in which absorbed photons are converted into phytoplankton biomass (ϕ_μ) tracks Chl : C_{Phyto}, the seasonal amplitude is comparatively muted (0.011 and 0.008 mol C (mol photons)$^{-1}$ in December and June, respectively) relative to the larger changes in Q_{PAR}.

5. Conclusions

We have presented a mechanistic NPP model that captures the greatest variance and has the lowest bias when compared to direct field measurements. This new model parses NPP into three functional traits: the amount of energy absorbed, the fraction of absorbed energy passed to the photosynthetic reaction centers, and the efficiency with which absorbed energy is converted to carbon biomass. Variations in absorbed energy drive large changes in NPP and growth through space and time and can be readily measured from satellite- and field-based methods. This research has also shown that the conversion of absorbed energy into carbon biomass appears to be largely constrained across the global ocean. Global oceanic NPP from the CAFE model (52 Pg C m^{-2} yr^{-1}) derived from climatological satellite data is similar to other model estimates, though the CAFE model predicts large differences in the spatial and temporal nature of NPP relative to other widely cited models. This result has important implications for estimated carbon fluxes to the deep ocean export as well as trophic transfer to higher organisms.

Future advances in satellite instrumentation and attendant algorithms can further enhance the accuracy of NPP measurements from space [*Z. Lee et al.*, 2015]. For example, hyperspectral ocean color measurements will likely improve $a_\phi(\lambda)$ assessments and have the potential to further improve phytoplankton community composition discrimination from space. Improved IOP measurements can be readily implemented into the current CAFE model, while taxonomic information may help constrain the physiological component (ϕ_μ) of the model. The accuracy of chlorophyll fluorescence efficiency $\left(\phi_f^{app}\right)$ measurements from space also requires precise knowledge of $a_\phi(\lambda)$ [*Huot et al.*, 2013]. Though not currently implemented in the CAFE model,

ϕ_f^{app} measurements may provide a mechanism to elucidate nutrient limitation from space [*Behrenfeld et al.*, 2009], and a robust evaluation of such measurements in the context of NPP is warranted. Finally, satellite-based light and detection ranging (lidar) data could provide data on the vertical structure of phytoplankton biomass [*Westberry and Behrenfeld*, 2013]. These data could supplement the growing capabilities of BIO-ARGO data to enhance our understanding of phytoplankton dynamics beneath the surface mixed layer.

Acknowledgments
Data from this study are available through the NASA ocean color Web portal (http://oceancolor.gsfc.nasa.gov/cgi/l3), Oregon State University's ocean productivity website (http://www.science.oregonstate.edu/ocean.productivity/), the Bermuda Atlantic Time Series Study (http://bats.bios.edu/), the Hawaii Ocean Time Series Study (http://hahana.soest.hawaii.edu/hot/hot-dogs/), and Arabian Sea Joint Global Ocean Flux Study (http://www1.whoi.edu/jgofs.html). The PPARR net primary production data set is available as a supplementary file to *Saba et al.* [2011]. This research is supported by the NASA grant NNH13ZDA001N-TERAQ (The Science of Terra and Aqua) awarded to T.K.W. The acquisition of BIOSOPE data was funded through CNRS(1)-INSU(2) grants. We kindly acknowledge David Antoine and Bernard Gentili for providing the source code to run the AM96 model as well as two anonymous reviewers whose comments improved this manuscript.

References

Antoine, D., and A. Morel (1996), Ocean primary production: 1. Adaptation of a spectral light-photosynthesis model in view of application to satellite chlorophyll observations, *Global Biogeochem. Cycles*, *10*, 43–55, doi:10.1029/95GB02831.

Babin, M., A. Morel, H. Claustre, A. Bricaud, Z. Kolber, and P. G. Falkowksi (1996), Nitrogen and irradiance-dependent variations of the maximum quantum yield of carbon fixation in eutrophic, mesotrophic and oligotrophic systems, *Deep Sea Res., Part I*, *43*, 1241–1272.

Behrenfeld, M. J., and E. S. Boss (2014), Resurrecting the ecological underpinnings of ocean plankton blooms, *Annu. Rev. Mar. Sci.*, *6*, 167–194, doi:10.1146/annurev-marine-052913-021325.

Behrenfeld, M. J., and P. G. Falkowski (1997), Photosynthetic rates derived from satellite-based chlorophyll concentration, *Limnol. Oceanogr.*, *42*, 1–20, doi:10.4319/lo.1997.42.1.0001.

Behrenfeld, M. J., O. Prasil, M. Babin, and F. Bruyant (2004), In search of a physiological basis for covariations in light-limited and light-saturated photosynthesis, *J. Phycol.*, *40*, 4–25, doi:10.1046/j.1529-8817.2004.03083.x.

Behrenfeld, M. J., E. Boss, D. A. Siegel, and D. M. Shea (2005), Carbon-based ocean productivity and phytoplankton physiology from space, *Global Biogeochem. Cycles*, *19*, GB1006, doi:10.1029/2004GB002299.

Behrenfeld, M. J., K. Worthington, R. M. Sherrell, F. P. Chavez, P. Strutton, M. McPhaden, and D. M. Shea (2006), Controls on tropical Pacific Ocean productivity revealed through nutrient stress diagnostics, *Nature*, *442*, 1025–1028, doi:10.1038/nature05083.

Behrenfeld, M. J., K. H. Halsey, and A. J. Milligan (2008), Evolved physiological responses of phytoplankton growth to their integrated growth environment, *Phil. Trans. R. Soc. B.*, *363*, 2687–2703, doi:10.1098/rstb.2008.0019.

Behrenfeld, M. J., et al. (2009), Satellite-detected fluorescence reveals global physiology of ocean phytoplankton, *Biogeosciences*, *6*, 779–794, doi:10.5194/bg-6-779-2009.

Behrenfeld, M. J., R. T. O'Malley, E. S. Boss, T. K. Westberry, J. R. Graff, K. H. Halsey, A. J. Milligan, D. A. Siegel, and M. B. Brown (2016), Revaluating ocean warming impacts on global phytoplankton, *Nat. Clim. Change*, *6*, 3223–3330.

Brewin, R. J. W., S. Sathyendranath, T. Hirata, S. J. Lavender, R. M. Barciela, and N. J. Hardman-Mountford (2010), A three-component model pf phytoplankton size class for the Atlantic Ocean, *Ecol. Model.*, *221*, 1472–1483, doi:10.1016/j.ecolmodel.2010.02.014.

Brewin, R. J., et al. (2015), The ocean colour climate change initiative: III. A round-robin comparison on in-water bio-optical algorithms, *Remote Sens. Environ.*, *162*, 271–294, doi:10.1016/j.rse.2013.09.016.

Bricaud, A., M. Babin, and H. Claustre (1995), Variability in the chlorophyll-specific absorption coefficients of natural phytoplankton: Analysis and parameterization, *J. Geophys. Res.*, *100*, 13,321–13,332, doi:10.1029/95JC00463.

Bricaud, A., A. Morel, M. Babin, K. Allali, and H. Claustre (1998), Variations of light absorption by suspended particles with chlorophyll *a* concentration in oceanic (case 1) waters: Analysis and implications for bio-optical models, *J. Geophys. Res.*, *103*, 31,003–31,044, doi:10.1029/98JC02712.

Bricaud, A., H. Claustre, J. Ras, and K. Oubelkheir (2004), Natural variability of phytoplanktonic absorption in oceanic waters: Influence of the size structure of algal populations, *J. Geophys. Res.*, *109*, C11010, doi:10.1029/20004JC00219.

Browning, T. J., H. A. Bouman, and C. M. Moore (2014), Satellite-detected fluorescence: Decoupling nonphotochemical quenching from iron stress signals in the South Atlantic and Southern Ocean, *Global Biogeochem. Cycles*, *2014*, 510–524, doi:10.1002/2013GB004773.

Carr, M. E., et al. (2006), A comparison of global estimates of marine primary production from ocean color, *Deep Sea Res., Part II*, *53*, 741–770, doi:10.1016/j.dsr2.2006.01.028.

Claustre, H., A. Sciandra, and D. Vaulot (2008), Introduction to the special section bio-optical and biogeochemical conditions in the South East Pacific in late 2004: The BIOSOPE program, *Biogeosciences*, *5*, 679–691.

Cullen, J. J. (2015), Subsurface chlorophyll maximum layers: Enduring enigma or mystery solved?, *Annu. Rev. Mar. Sci.*, *7*, 207–239, doi:10.1146/annurev-marine-010213-135111.

de Boyer Montégut, C., G. Madec, A. S. Fischer, A. Lazar, and D. Iudicone (2004), Mixed layer depth over the global ocean: An examination of profile data and a profile-based climatology, *J. Geophys. Res.*, *109*, C12003, doi:10.1029/2004JC002378.

Dierssen, H., G. B. McManus, A. Chlus, D. Qiu, B.-C. Gao, and S. Lin (2015), Space station image captures a red tide ciliate bloom at high spectral and spatial resolution, *Proc. Natl. Acad. Sci. U.S.A.*, *112*, 14,783–14,787, doi:10.1073/pnas.1512538112.

Friedrichs, M. A. M., et al. (2009), Assessing the uncertainties of model estimates of primary productivity in the tropical Pacific Ocean, *J. Mar. Syst.*, *76*, 113–133, doi:10.1016/j.jarsys.2008.05.010.

Geider, R. J., H. L. MacIntyre, L. M. Graziano, and R. M. L. McKay (1998), Responses of the photosynthetic apparatus of *Dunaliella tertiolecta* (Chlorphyceae) to nitrogen and phosphorus limitation, *Eur. J. Phycol.*, *33*, 315–322, doi:10.1080/09670269810001736813.

Graff, J. R., T. K. Westberry, A. J. Milligan, M. B. Brown, G. Dall'Olmo, V. van Dongen-Vogels, K. M. Reifel, and M. J. Behrenfeld (2015), Analytical phytoplankton carbon measurements spanning diverse ecosystems, *Deep Sea Res., Part I*, *102*, 16–25, doi:10.1016/j.dsr.2015.04.006.

Halsey, K. H., and B. M. Jones (2015), Phytoplankton strategies for photosynthetic energy allocation, *Annu. Rev. Mar. Sci.*, *7*, 265–297, doi:10.1146/annurev-marine-010814-015813.

Halsey, K. H., A. J. Milligan, and M. J. Behrenfeld (2010), Physiological optimization underlies growth rate-independent chlorophyll-specific gross and net primary production, *Photosynth. Res.*, *103*, 125–137.

Halsey, K. H., A. J. Milligan, and M. J. Behrenfeld (2011), Linking time-dependent carbon-fixation efficiencies in *Dunaliella tertiolecta* (Chlorophycaea) to underlying metabolic pathways, *J. Phycol.*, *47*, 66–76.

Halsey, K. H., A. J. Milligan, and M. J. Behrenfeld (2014), Contrasting strategies of photosynthetic energy utilization drive lifestyle strategies in ecologically important picoeukaryotes, *Metabolites*, *4*, 260–280, doi:10.3390/metabo4020260.

Hendricks, M. B., M. L. Bender, and B. A. Barnett (2005), Triple oxygen isotope composition of dissolved O_2 in the equatorial Pacific: A tracer of mixing, production, and respiration, *J. Geophys. Res.*, *110*, C12021, doi:10.1029/2004JC002735.

Hu, C., Z. Lee, and B. Franz (2012), Chlorophyll *a* algorithms for oligotrophic oceans: A novel approach based on three-band reflectance difference, *J. Geophys. Res.*, *117*, C010011, doi:10.1029/2011JC007395.

Huot, Y., and M. Babin (2010), Overview of fluorescence protocols: Theory, basic concepts and practice, in *Chlorophyll a Fluorescence in Aquatic Sciences: Methods and Applications*, edited by D. J. Suggett, O. Prasil, and M. A. Borowitzka, chap. 3, pp. 31–74, Springer, Berlin.
Huot, Y., et al. (2008), Relationship between photosynthetic parameters and different proxies of phytoplankton biomass in the subtropical ocean, *Biogeosciences*, *4*, 853–868, doi:10.5194/bg-4-853-2007.
Huot, Y., B. A. Franz, and M. Fradette (2013), Estimating variability in the quantum yield of Sun-induced chlorophyll fluorescence: A global analysis of oceanic waters, *Remote Sens. Environ.*, *132*, 238–253, doi:10.1016/j.rse.2013.01.003.
International Ocean-Colour Coordinating Group (2006), Remote sensing of inherent optical properties: Fundamentals, tests of algorithms, and applications, in *Reports of the International Ocean-Colour Coordinating Group*, edited by Z.-P. Lee, No. 5, IOCCG, Dartmouth, Canada.
Intergovernmental Panel on Climate Change (IPCC) (2013), *Climate Change 2013: The Physical Science Basis. Contribution of Working Group I to the Fifth Assessment Report of the Intergovernmental Panel on Climate Change*, edited by T. F. Stocker et al., pp. 1535, Cambridge Univ. Press, Cambridge, U. K., and New York.
Jakob, T., U. Schreiber, V. Kirchesch, V. Langer, and C. Wilhelm (2007), A complete energy balance from photons to new biomass reveals a light- and nutrient-dependent variability in the metabolic costs of carbon assimilation, *J. Exp. Bot.*, *58*, 2101–2112.
Kahru, M., M. G. Jacox, Z. Lee, R. M. Kudela, M. Manzano-Sarabia, and B. G. Mitchell (2015), Optimized multi-satellite merger of primary production estimates in the California Current using inherent optical properties, *J. Mar. Sys.*, *147*, 94–102, doi:10.1016/j.jmarsys.2014.06.003.
Kiefer, D. A., and B. G. Mitchell (1983), A simple, steady-state description of phytoplankton growth based on absorption cross section and quantum efficiency, *Limnol. Oceanogr.*, *28*, 770–776, doi:10.4319/lo.1983.28.4.0770.
Laws, E. A., and T. T. Bannister (1980), Nutrient and light-limited growth of *Thalassiosira fluvaitilis* in continuous culture, with implications for phytoplankton growth in the ocean, *Limnol. Oceanogr.*, *25*, 457–473.
Lee, Y. J., et al. (2015), An assessment of phytoplankton primary productivity in the Arctic Ocean from satellite ocean color/in situ chlorophyll-*a* based models, *J. Geophys. Res. Oceans*, *120*, 6508–6541, doi:10.1002/2015JC011018.
Lee, Z., K. L. Carder, and R. A. Arnone (2002), Deriving inherent optical properties from water color: A multiband quasi-analytical algorithm for optically deep waters, *Appl. Optics.*, *41*, 5722–5755.
Lee, Z., K. Du, and R. Arnone (2005), A model for the diffuse attenuation coefficient of downwelling irradiance, *J. Geophys. Res.*, *110*, C02016, doi:10.1029/2004JC002275.
Lee, Z., et al. (2011), An assessment of optical properties and primary production derived from remote sensing in the Southern Ocean (SO GasEx), *J. Geophys. Res.*, *118*, 4241–4255, doi:10.1002/jgrc.20308.
Lee, Z., J. Marra, M. J. Perry, and M. Kahru (2015), Estimating oceanic primary productivity from ocean color remote sensing: A strategic assessment, *J. Mar. Syst.*, *149*, 50–59, doi:10.1016/j.marsys.2014.11.015.
Lee, Z. P., K. L. Carder, J. Marra, R. G. Steward, and M. J. Perry (1996), Estimating primary productivity at depth from remote sensing, *Appl. Opt.*, *35*, 463–474, doi:10.1364/SO.35.000463.
Levitus, S. (1982), Climatological atlas of the world ocean. *NOAA Prof. Pap. 13*, 173 pp.
Lin, H., F. I. Kuzminov, J. Park, S. Lee, P. G. Falkowski, and M. Y. Gorbunov (2016), The fate of photons absorbed by phytoplankton in the global ocean, *Science*, *351*, 264–267, doi:10.1126/science.aab2213.
Lochte, K., H. W. Ducklow, M. J. R. Fasham, and C. Stienen (1993), Plankton succession and carbon cycling at 47°N 20°W during the JGOFS North Atlantic Bloom Experiment, *Deep Sea Res., Part II*, *40*, 91–114.
MacIntyre, H. L., T. M. Kana, T. Anning, and R. J. Geider (2002), Photoacclimation of photosynthesis irradiance response curves and photosynthetic pigments in microalgae and cyanobacteria, *J. Phycol.*, *38*, 17–38.
Marañón, E., P. Cermeño, M. Latasa, and R. D. Tadonkéké (2012), Temperature, resources, and phytoplankton size structure in the ocean, *Limnol. Oceanogr.*, *57*, 1266–1278, doi:10.4319/lo.2012.57.5.1266.
Maritorena, S., D. A. Siegel, and A. R. Peterson (2002), Optimization of a semianalytical ocean color model for global-scale applications, *Appl. Optics.*, *41*, 2705–2714, doi:10.1364/AO.41.002705.
Markager, S., and W. F. Vincent (2001), Light absorption by phytoplankton: Development of a matching parameter for algal photosynthesis under different spectral regimes, *J. Plank. Res.*, *23*, 1373–1384, doi:10.1093/plankt/23.12.1373.
Marra, J. (2002), Approaches to the measurement of plankton production, in *Phytoplankton Productivity: Carbon Assimilation in Marine and Freshwater Ecosystems*, edited by P. J. L. Williams, D. N. Thomas, and C. S. Reynolds, pp. 78–108, Blackwell, Malden, Mass.
Marra, J., C. Ho, and C. Trees (2003), An alternative algorithm for the calculation of primary productivity from remote sensing data, LDEO Technical Report, LDEO-2003-1.
Marra, J., C. Trees, and J. E. O'Reilly (2007), Phytoplankton pigment absorption: A strong predictor of primary productivity in the surface ocean, *Deep Sea Res., Part I*, *54*, 155–163, doi:10.1016/j/dsr.2006.12.001.
Mignot, A., H. Claustre, J. Uitz, A. Poteau, F. D'Ortenzio, and X. Xing (2014), Understanding the seasonal dynamics of phytoplankton biomass and the deep chlorophyll maximum in oligotrophic environments: A Bio-Argo float investigation, *Global Biogeochem. Cycles*, *28*, 856–876, doi:10.1102/2013GB004871.
Milutinovic, S., and L. Bertino (2011), Assessment and propagation of uncertainties in input terms through an ocean-color based model of primary productivity, *Remote Sens. Environ.*, *115*, 1906–1917, doi:10.1016/j.rse.2011.03.013.
Morel, A., and J. F. Berthon (1989), Surface pigments, algal biomass profiles, and potential production of the euphotic layer: Relationships reinvestigated in view of remote-sensing applications, *Limnol. Oceanogr.*, *34*, 1545–1562, doi:10.4319/lo.1989.34.8-1545.
Morel, A., D. Antoine, M. Babin, and Y. Dandoneau (1996), Measured and modeled primary production in the northeast Atlantic (EUMELI JGOFS program): The impact of natural variations in photosynthetic parameters on model predictive skill, *Deep Sea Res., Part I*, *43*, 1273–1304, doi:10.1016/0967-0637(96)00059-3.
Ondrusek, M. E., R. R. Bidigare, K. Waters, and D. M. Karl (2001), A predictive model for estimating rates of primary production in the subtropical North Pacific Ocean, *Deep Sea Res., Part II*, *48*, 1837–1863.
Pope, R. M., and E. S. Fry (1997), Absorption spectrum (380–700 nm) of pure water. II. Integrating cavity measurements, *Appl. Optics*, *36*, 8710–8723.
Saba, V. S., et al. (2010), Challenges of modelling depth-integrated marine productivity over multiple decades: A case study at BATS and HOT, *Global Biogeochem. Cycles*, *24*, GB3020, doi:10.1029/2009GB003655.
Saba, V. S., et al. (2011), An evaluation of ocean color model estimates of marine primary productivity in coastal and pelagic regions across the globe, *Biogeosciences*, *8*, 489–503, doi:10.5194/bg-8-489-2011.
Silsbe, G. M., and J. C. Kromkamp (2012), Modeling the irradiance dependency of the quantum efficiency of photosynthesis, *Limnol. Oceanogr. Methods*, *10*, 645–652, doi:10.4319/lom.2012.10.645.

Silsbe, G. M., and S. Y. Malkin (2016), Where light and nutrients collide: The global distribution and activity of subsurface chlorophyll maximum layers, in *Aquatic Microbial Ecology and Biogeochemistry: A Dual Perspective*, edited by P. M. Glibert and T. M. Kana, pp. 141–152, Springer, Berlin, Germany.

Smyth, T. J., G. H. Tilstone, and S. B. Groom (2005), Integration of radiative transfer into satellite models of ocean primary production, *J. Geophys. Res.*, *110*, C10014, doi:10.1029/2004JC002784.

Suggett, D. J., C. Mark Moore, A. E. Hickman, and R. J. Geider (2009), Interpretation of fast repetition rate (FRR) fluorescence: Signatures of phytoplankton community structure versus physiological state, *Mar. Ecol. Prog. Ser.*, *376*, 1–19, doi:10.3354/meps07830.

Uitz, J., H. Claustre, A. Morel, and S. B. Hooker (2006), Vertical distribution of phytoplankton communities in open ocean: An assessment based on surface chlorophyll, *J. Geophys. Res.*, *111*, C08005, doi:10.1029/2005JD003207.

Uitz, J., Y. Huot, F. Buyant, M. Babin, and H. Claustre (2008), Relating phytoplankton photophysiological properties to community structure on large scales, *Limnol. Oceanogr.*, *53*, 614–630.

Werdell, P. J., et al. (2013), Generalized ocean color inversion model for retrieving marine inherent optical properties, *Appl. Opt.*, *52*, 2019–2037, doi:10.1364/AO.52.002019.

Westberry, T. K., and M. J. Behrenfeld (2013), Oceanic net primary production, in *Biophysical Applications of Satellite Remote Sensing*, edited by J. M. Hanes, chap. 8, pp. 205–230, Springer, Berlin, Germany.

Westberry, T. K., and D. A. Siegel (2003), Phytoplankton natural fluorescence variability in the Sargasso Sea, *Deep Sea Res., Part I*, *50*, 417–434, doi:10.1016/S0967-0637(03)00019-0.

Westberry, T. K., M. J. Behrenfeld, D. A. Siegel, and E. Boss (2008), Carbon-based primary productivity modeling with vertically resolved photoacclimation, *Global Biogeochem. Cycles*, *22*, GB2024, doi:10.1029/2007GB003078.

Westberry, T. K., P. Schultz, M. J. Behrenfeld, J. P. Dunne, M. R. Hiscock, S. Maritorena, J. L. Sarmeinto, and D. A. Siegel (2016), Annual cycles of phytoplankton biomass in the subarctic Atlantic and Pacific Ocean, *Global Biogeochem. Cycles*, *30*, 175–190, doi:10.1002/2015GB005276.

Wozniak, B., J. Dera, and O. J. Koblentz-Mishke (1992), Modeling the relationship between primary production, optical properties and nutrients in the sea (as a basis for indirectly estimating phytoplankton production), Ocean Opt. 11, Proc. *SPIE Int. Soc. Opt. Eng.* 1750-246-275.

Zhang, X., and L. Hu (2009), Estimating scattering of pure water from density fluctuation of the refractive index, *Optics Express*, *17*, 1671–1678.